Palaeogeography, Palaeoclimatology, Palaeoecology 680 (2025) 113368

Contents lists available at ScienceDirect

Palaeogeography, Palaeoclimatology, Palaeoecology

journal homepage: www.elsevier.com/locate/palaeo

Magnetobiochronology of the Izaga section (South Pyrenean Foreland basin): Implications for defining the global boundary stratotype section and point (GSSP) of the Bartonian Stage and unravelling climate change across the Middle Eocene Climate Optimum

P. Sierra-Campos [a,*], G. Bernaola [b], P. Calvín [c], M. Montes [d], A. Luzón [e], E. Bellido [d], A. Payros [f], E. Beamud [g], B. Oliva-Urcia [e], E.L. Pueyo [a], J.C. Larrasoaña [a,h]

[a] CN IGME, CSIC, Unidad de Zaragoza, Zaragoza, Spain
[b] Department of Mining Engineering and Metallurgy and Materials Science, Faculty of Engineering Bilbao, University of the Basque Country (UPV/EHU), Plaza Ingeniero Torres Quevedo 1, E-48013 Bilbao, Spain
[c] Departamento de Geología, Universidad de Salamanca, Salamanca, Spain
[d] CN IGME, CSIC, Madrid, Spain
[e] Geotransfer-IUCA, Departamento de Ciencias de la Tierra, Universidad de Zaragoza, Zaragoza, Spain
[f] Department of Geology, Faculty of Science and Technology, University of the Basque Country (UPV/EHU), Ap. 644, E-48080 Bilbao, Spain
[g] Paleomagnetic Laboratory CCiTUB-GEO3BCN CSIC, 08028 Barcelona, Spain
[h] Departamento de Ciencias, Universidad Pública de Navarra, Pamplona, Spain

ARTICLE INFO

Editor: Howard Falcon-Lang

Keywords:
South Pyrenean basin
Magnetostratigraphy
Calcareous nannofossil biostratigraphy
Bartonian
GSSP
C19n
MECO

ABSTRACT

We present a new magnetobiostratigraphic study of the Izaga composite section (South Pyrenean foreland basin), performed to investigate the possibility of defining the Bartonian GSSP and to assess the yet unexplored sedimentary expression of the Middle Eocene Climate Optimum (MECO) in the deep palaeoenvironments of the basin. Our results indicate that the section spans from the uppermost part of Chron C19r to the uppermost part of C18n.2n, comprising calcareous nannofossil biozones CNE14 and CNE15. As found in most prospective sections studied previously, the occurrence of delayed magnetizations has prevented precise delineation of the marker of the Bartonian GSSP, the short lived Chron C19n, which reinforces the idea that an alternative biostratigraphic event might need to be chosen as the primary marker of the GSSP. In this regard, we propose the highest occurrence of *Sphenolithus furcatolithoides* B, whose persistent location close to the top of C19n has been corroborated at the Izaga composite section. If this datum accepted, the Izaga composite section can be regarded as one of the best prospective successions to host the Bartonian GSSP due to its expanded nature and superb outcrop conditions. Our results also reveal an increase in the input of reworked calcareous nannofossils and organic matter of continental origin concurring with a negative shift in the carbonate carbon and oxygen stable isotope record around the C19r/C18n.2n boundary, and hence demonstrate that the enhanced hydrological cycle induced by the MECO is manifested along a complete continental to deep marine transect along the South Pyrenean basin.

1. Introduction

The base of the Bartonian stage is the only Paleogene Global Stratotype Section and Point (GSSP) that is still pending definition (Speijer et al., 2020; https://www.paleogene.org/working-group/bartonian/), mainly due to the lack of sections that satisfy the geological and logistic requirements of the International Commission on Stratigraphy (see Remane et al., 1996). The name "Bartonian" was used for the first time by Prestwich (1847) and later by Mayer-Eymar (1858) to refer to the Barton clays and sands exposed at Barton-On-Sea in the Hampshire

* Corresponding author.
E-mail addresses: p.sierra@igme.es (P. Sierra-Campos), gilen.bernaola@ehu.eus (G. Bernaola), pcalvin@usal.es (P. Calvín), m.montes@igme.es (M. Montes), aluzon@unizar.es (A. Luzón), e.bellido@igme.es (E. Bellido), a.payros@ehu.eus (A. Payros), betbeamud@ub.edu (E. Beamud), boliva@unizar.es (B. Oliva-Urcia), unaim@igme.es (E.L. Pueyo), jc.larra@igme.es (J.C. Larrasoaña).

https://doi.org/10.1016/j.palaeo.2025.113368
Received 28 February 2025; Received in revised form 12 July 2025; Accepted 20 October 2025
Available online 24 October 2025

Basin, southern England. The first proposal to define the base of the Bartonian stage was made by Keeping (1887) who proposed a level rich in *Nummulites prestwichianus*. This level is located in the upper part of calcareous nannofossil zone NP16 (Martini, 1971) towards the middle part of Chron C18r (Dawber et al., 2011; Hooker and King, 2019). Currently, the International Commission on Stratigraphy provisionally places the base of the Bartonian stage close to the LAD (Last Appearance Datum) of the calcareous nannofossil *Reticulofenestra reticulata* in the Contessa Highway section, but this event could be unsuitable due to its diachronism between low-mid latitudes and southern high latitudes (Berggren et al., 1995; Messaoud et al., 2021). There are not distinctive biostratigraphic events close to the interval potentially corresponding to the base of Bartonian and different markers have been proposed. The top of magnetic polarity Chron C19n has been proposed to be the most useful marker for its GSSP (Jovane et al., 2010; Speijer et al., 2020). Unfortunately, one of the sections where Chron C19n has been more accurately identified (Contessa Highway section in Italy; Jovane et al., 2007, 2010) is located at the entrance of an active quarry, where free access, the possibility of fixing a permanent marker, and the long-term protection of the site cannot be granted. Another Italian prospective section, the Bottaccione section, is affected by delayed remanence acquisition processes and by an important shift in sedimentation rates across the Lutetian/Bartonian transition, which have resulted in a poor delineation of Chron C19n (Coccioni et al., 2022) (Fig. 1a). A similar problem affects the Oyambre section in northern Spain, where delayed magnetizations have seemingly resulted in the erasure of Chron C19n

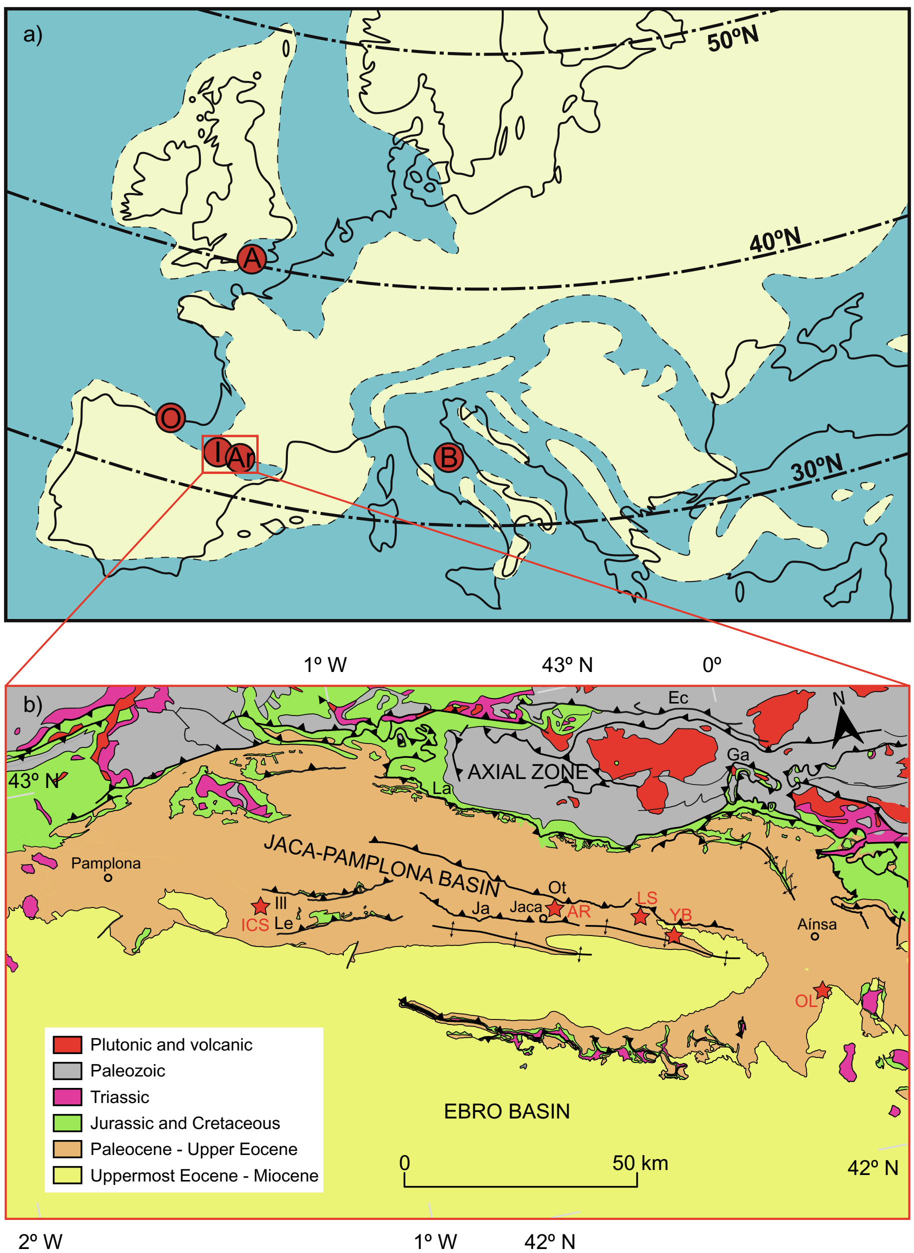

Fig. 1. a) Location of prospective Bartonian GSSP sections (modified from Plaziat, 1981): (A) Alum Bay section (Cotton et al., 2021); (B) Bottaccione section (Coccioni et al., 2022), also Contessa Highway (Jovane et al., 2007, 2010) is located in the same area; (O) Oyambre section (Payros et al., 2015a); (Ar) Aragón section (Oms et al., 2003); (I) Izaga section (this study). b) Geological map of the studied area with location of the new magnetostratigraphic section (ICS) and other sections of interest. AR: Aragón section (Oms et al., 2003); LS: Latas section (Lasluisa et al., 2024); OL: Olsón section (Vinyoles et al., 2021); YB: Yebra de Basa section (Vinyoles et al., 2021; Peris-Cabré et al., 2023). Ill: Illón thrust; Ot: Oturia thrust; Ja: Jaca thrust; Le: Leire thrust; La: Larra thrust; Ga: Gavarnie thrust; Ec: Eaux-Chaudes thrust.

(Payros et al., 2015a) (Fig. 1a). The Aragón section in the Spanish Pyrenees has been shown to record Chron C19n, but it is also poorly delineated given the relatively poor paleomagnetic quality and outcrop conditions, and the presence of frequent and thick channelized erosive turbidites, across the interval of interest (Oms et al., 2003) (Fig. 1a). A final prospective section at Alum Bay (UK), considered as the classic reference section for the Bartonian, has yielded inconclusive magnetostratigraphic results linked to tectonic disturbances, which has resulted in a somehow ambiguous identification of Chron C19n that appears, in any case, incomplete (Cotton et al., 2021) (Fig. 1a). Overall, it seems that new areas need to be searched in order to locate prospective sections and open the range of possibilities for defining the Bartonian GSSP.

One of such locations is the Jaca-Pamplona Basin in the western part of the South Pyrenean foreland basin (SPFB), an area well-known for the presence of expanded Eocene successions deposited in a deep marine environment (see Payros et al., 2015a; Barnolas et al., 2019). Although initial surveys aimed at analysing the potential of the area for establishing the Bartonian GSSP produced negative results given the overall poor-exposure conditions (Payros et al., 2014, 2015a), recent efforts have enabled the identification of a thick (>1100 m) succession of hemipelagic marls and minor distal turbidites that includes all the formations recognized in the SPFB spanning the upper part of the Lutetian and the whole Bartonian (Puigdefábregas, 1975; Remacha et al., 1987, 1998; Payros, 1997; Payros et al., 1999; Garcés et al., 2020; Roigé et al., 2023). Especially relevant is the straightforward lithostratigraphic correlation of this new section, named Izaga, with the upper half part of the neighbouring Aragón section (Oms et al., 2003), which spans from Chron C19r to C18n and, hence, includes Chron C19n. The more distal position of the Izaga section, along with its superb exposure and free access conditions, make it an ideal candidate to host the marker of the Bartonian GSSP provided it can produce a good quality record of Chron C19n. In addition to that, the Izaga section can also be of especial palaeoclimatic significance because it is also expected to span the Middle Eocene Climate Optimum (MECO), a global warming event occurred around the C18r/C18n boundary that has been associated with enhanced continental runoff and a concomitant progradation of deltaic sedimentation in the eastern part of the Jaca-Pamplona Basin (Peris-Cabré et al., 2023; Lasluisa et al., 2024).

In this work we present a new magnetostratigraphic study of the Izaga section, which is combined with novel biostratigraphic and palaeoenvironmental data based on calcareous nannofossils and carbon and oxygen stable isotope analyses. This study has enabled us: 1) to provide an improved age model for the Lutetian/Bartonian marine sediments of the western SPFB and to discuss their bearings on the definition of the Bartonian GSSP; and 2) to examine the sedimentary expression of the MECO in the distal part of the SPFB and, hence, complete the knowledge of its effects on the sedimentation along a continental to deep marine transect across the SPFB.

2. Geological setting

The Pyrenees constitute a linear, asymmetric, double vergency mountain belt formed at the boundary between the Iberian and the European plates. From the Late Cretaceous to the Miocene, the convergence, collision and subduction of Iberia underneath Europe caused the end of sea floor spreading in the Bay of Biscay and the initiation of compression along the northern Iberian margin, which led to the inversion of the Pyrenean hyperextended rift system and, ultimately, to the uplift of the Pyrenees (Choukroune, 1992; Muñoz, 1992, 2002; Pedrera et al., 2023). The Jaca-Pamplona Basin represents the westernmost part of the SPFB (central Pyrenees) (Fig. 1b), whose Cenozoic rocks record the evolution of the basin within the framework of the tectonic development of the Pyrenean range. A thin (<300 m-thick) Paleocene-lowermost Eocene sequence, made up of limestones and marls, indicates sedimentation in a shallow marine area during a period of tectonic stability that preceded development of the SPFB (Payros et al., 1999; Labaume et al., 2016). The emplacement of the Lakora-Eaux-Chaudes and Larra-Monte Perdido thrust systems to the north during the early-middle Eocene drove rapid deepening of the newly-born SPFB and the establishment of an axial turbiditic system ultimately fed from the emerging areas of the South Pyrenean Central Unit to the east. This system is represented by up to 4500 m of hemipelagic marls and turbiditic sandstones that constitute the Hecho Group (Mutti et al., 1972), which also includes the so-called South Pyrenean Eocene carbonate megaturbidites, megabeds or megabreccias (MT, Labaume et al., 1983; MB Barnolas and Teixell, 1994; SPECM, Payros et al., 1999). These megabreccias are thick (up to 200 m) and extensive (>130 km along strike) beds that represent the massive redeposition of platform sediments in a deep basinal setting triggered by the rapid oversteepening and collapse of the forebulge of the basin (e.g., its southern margin) in response to tectonic loading on its active northern margin (Barnolas and Teixell, 1994; Payros et al., 1999). As deformation migrated towards the foreland, the activity of the Gavarnie thrust and its splays into the cover (Oturia and Jaca thrusts) between the late Eocene and the early Oligocene occurred synchronously with the westward progradation of the sedimentary systems, which evolved first to prodeltaic deposits (Larrés, Urroz-Sabiñánigo and Pamplona formations, up to 500, 150 and 2000 m thick, respectively), later to deltaic sandstones (Belsué-Atarés and Guendulain formations, <400 m thick) and, eventually, to continental mudstones and sandstones (lower part of the Campodarbe Formation, <2000 m) (Puigdefábregas, 1975; Montes, 2009; Oliva-Urcia et al., 2019). Ongoing tectonic deformation during this period led to the development of a pressure-solution cleavage domain and an associated remagnetization event that affects the northern fringe of the Jaca-Pamplona Basin (Oliva-Urcia et al., 2008; Izquierdo-Llavall et al., 2013). Later deformation led to the southward displacement of the basin atop the most external thrust unit, the Guarga thrust, a process that is recorded by the sedimentation of the overlying upper part of the Campodarbe and Uncastillo formations (late Oligocene-early Miocene) (Millán et al., 1995, 2000).

The Izaga section is located in the northern limb of the eastern termination of the Izaga syncline, which represents the broad synclinorium that characterizes the Jaca-Pamplona Basin in its western sector. There, the syncline axis shows a gentle (<6°) dipping to the WNW that is caused by the uplift of its easternmost continuation at the hanging wall of the Leire thrust (Larrasoaña et al., 2003a, 2004). The section is located >8 km ahead of the cleavage and remagnetization fronts that affect the northern fringe of the basin, which run along a NW-SE direction that is oblique to the trace of the Illón thrust located further north (Fig. 1b) (Izquierdo-Llavall et al., 2013, 2015). The section includes from the uppermost part of the Hecho Group (Jaca Turbidites) to the lowermost levels of the Pamplona Marls Formation (Fig. 2).

3. Materials and methods

3.1. Stratigraphy and sedimentology of the Izaga section

The Izaga section was sampled across the badlands located in the vicinity of Nardués-Andurra village (base: 42° 42' 37.95" N. 1° 15' 43.12" W; top: 42° 41' 49.57" N. 1° 17' 12.42" W). (Fig. 2). It is composed of two parts, a short (147 m) subsection named Berroya and a long (1016 m) subsection named Nardués-Andurra, which are located about 2 km away from each other. We have logged and described the lithology, colour, grain size and sedimentary structures and texture of sediments along the two subsections. Their thickness was measured with a Jacob's staff and the bedding attitude along the profile was measured with a compass. This methodology has allowed a reliable correlation between the two subsections, which is fully supported by cartographic criteria, and the construction of a composite section of 1116 m. X-ray diffraction analyses of samples of special significance have been conducted with a Bruker D8 Advance ECO, following standard procedures, at the Universidad Pública de Navarra (UPNA) in order to determine

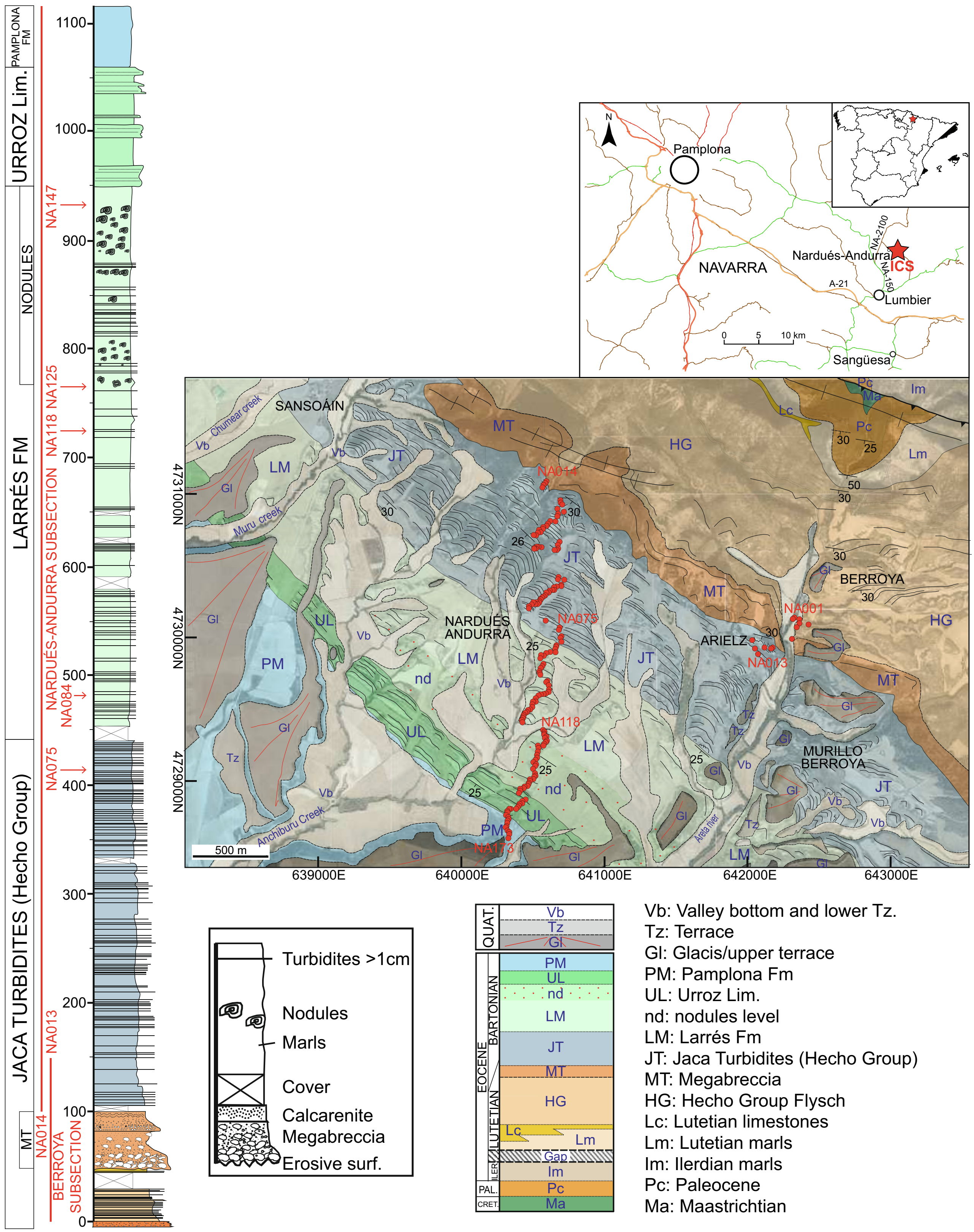

Fig. 2. Detailed geological map, illustrating the location of the sampling points (red dots) and the stratigraphic log with the different stratigraphic formations and the sampled subsections.

their main mineralogy.

3.2. Magnetostratigraphy and rock magnetic properties

A total of 173 magnetostratigraphic sites were evenly sampled with an average spacing of 6.5 m along the composite section and were geolocated using a GPS. At least two oriented paleomagnetic samples were collected at each site with a portable electrical power drill cooled by water. The cores were oriented in situ with a magnetic compass mounted on a core-orienting fixture and were later cut into paleomagnetic standard specimens. Once in the Paleomagnetic Laboratory of the Geo3BCN (CCiTUB–GEO3BCN-CSIC) in Barcelona, stepwise demagnetization and measurement of the natural remanent magnetization (NRM) of one specimen per site was performed through thermal (TH) demagnetization procedures using a furnace with separate heating and cooling chambers (ASC TD48EU, ASC Scientific). The NRM was measured with a superconducting rock magnetometer (2G Enterprises), which has a noise level of $< 7 \times 10^{-6}$ A/m, from room temperature to 500°C at up to eleven steps of 25°C-50°C. In each step, low-field magnetic susceptibility was measured using AGICO KLY-2 Kappabridge to detect the neoformation of magnetic minerals upon heating. Characteristic components directions (ChRM) were calculated by principal component analyses (PCA, Kirschvink, 1980) after they were identified through visual inspection of orthogonal demagnetization plots (Zijderveld, 1967) using the VPD software (Ramón et al., 2017). Fisher statistics (Fisher, 1953) were applied to ChRM using Stereonet software (Cardozo and Allmendinger, 2013), and the stability bootstrap reversal test (Tauxe et al., 1991) was conducted using PmagPy software (Tauxe et al., 2016).

Rock magnetic data were measured to provide insights into the magnetic carriers of the ChRM and into the palaeoenvironmental significance of the studied sedimentary sequence. A first set of data includes the measurement of non-destructive magnetic properties for one specimen per site, with the exception of 7 sites where no specimens were left after thermal demagnetization. These properties include: 1) the low-field magnetic susceptibility, which was measured with a KLY-3 Kappabridge (AGICO, Czech Republic) susceptibility meter; 2) an anhysteretic remanent magnetization (ARM), which was applied with a an alternating field (AF) Demagnetizer (D-Tech 2000, ASC Scientific) using an AF of 100 mT and a bias field of 0.05mT and was measured with a superconducting rock magnetometer (2G Enterprises); and 3) two isothermal remanent magnetizations ($IRM_{@0.3T}$ and $IRM_{@1.2T}$) applied with a pulse magnetizer (ASC IM10-30, ASC-Scientific) at fields of 0.3T and 1.2T, respectively, which were measured with the superconducting rock magnetometer. The low-field magnetic susceptibility (χ) was measured at the Magnetic Fabrics Laboratory of the Universidad de Zaragoza, whereas ARM and IRM measurements were conducted at the Paleomagnetic Laboratory of the Geo3BCN (CCiTUB–GEO3BCN-CSIC). Relevant parameters and interparametric ratios (IRM@1.2T and IRM@1.2T/χ) have been obtained from this data set to establish relative variations in the type, concentration and grain size of magnetic minerals in the studied sediments (see Liu et al., 2012).

A second set of analyses includes magnetic properties that involve invasive subsampling or destructive measurement of magnetic properties, which were applied to selected samples representative for the different paleomagnetic behaviours identified along the succession. Stepwise TH demagnetization of a three component IRM applied at fields of a 1.2 T, 0.3 T and 0.1 T was measured at the Paleomagnetic Laboratory of the Geo3BCN from room temperature to 600°C at 50°C steps in order to identify magnetic minerals on the basis of their unblocking temperatures and coercivities (Lowrie, 1990). Moreover, low-temperature experiments of sister samples were measured using a MPMS-XL7 (by Quantum Design) at the Laboratory of Magnetic Properties of the Universidad Pública de Navarra. Finally, thermomagnetic runs were measured with a KLY-3 at the Magnetic Fabrics Laboratory of the Universidad de Zaragoza and a KLY-4 at the Palaeomagnetiklabor Gams of the Montanuniversität Leoben.

3.3. Calcareous nannofossils

The calcareous nannofossil dataset is based on the analysis of 173 samples (6.3 m of average resolution), which were prepared as smear slides following standard methods (Bown and Young, 1998) and analyzed using a Zeiss Axioplan transmitted-light microscopy at 1600 magnification. Additionally, the smear-slides were also examined at 2500 magnification in order to detect smaller species, observe greater detail, and for photographic purposes.

The calcareous nannofossil study has been carried out in two rounds. In the first round, five tracks (14.7 mm^2) per sample were analyzed through the 173 samples to detect all the species of the original assemblage (see Appendix 1 and Plates 1-5 of the Supplementary material). In this first round, only the presence or absence of the different taxa was determined with the exception of *Reticulofenestra reticulata*, *Sphenolithus furcatolithoides* B and *Sphenolithus spiniger*, for which a specific count was carried out to determine their highest and lowest common occurrences.

In the second round, a quantitative study was carried out at a lower stratigraphic resolution (~22 m) on 50 of the 173 samples. A minimum of 300 autochthonous specimens were counted and identified per sample to determine the relative abundance of species and genera, which is expressed as percentage (%) of the total autochthonous assemblage. We estimated the absolute abundance of calcareous nannofossils as the ratio between the total autochthonous specimens and the total number of FOV (fields of view) examined for each sample (N/FOV). Taking into account that the area of a FOV at 1600 magnification is equal to ~0.0113 mm^2, the number of specimens per mm^2 was calculated and rounded up following standard practice. The reworked/autochthonous proportion was calculated by dividing the number of reworked specimens by the total number (autochthonous and reworked) of calcareous nannofossils. Mesozoic, Paleocene and early Eocene taxa that were extinct by Zone NP15 (Martini, 1971) times were classified as reworked specimens.

Calcareous nannofossils were determined using taxonomic concepts compiled in the updated online dataset Nannotax (https://www.mikrotax.org/Nannotax3/index.html), except for *Cribrocentrum*, *Dictyococcites* and *Reticulofenestra*, for which we followed Agnini et al. (2014). The biostratigraphic zonation is based on the schemes of Martini (1971), Okada and Bukry (1980), Fornaciari et al. (2010) and Agnini et al. (2014). Four types of biohorizons were defined. The lowest occurrence (LO) and the highest occurrence (HO) refer to the lowest and highest continuous occurrences of taxa, respectively. It was considered that the occurrence of a taxon is continuous when it appears in a series of successive samples, even if it may be absent in a few interspersed levels. The lowest common occurrence (LCO) and the highest common occurrence (HCO) of a species mark the levels where its abundance crosses the threshold of 5 specimens per mm^2. The LO, LCO, HC and HCO positions were defined at the midpoint between two successive samples, the possible margin of error being expressed by the stratigraphic distance to the closest underlying and overlying samples. Details on the preservation, reworking and abundances of the studied calcareous nannofossil assemblages are given in the Supplementary Material, which also includes a list of all the autochthonous taxa identified in the Izaga section and five plates where most of them are illustrated.

3.4. Carbonate carbon and oxygen stable isotopes

Carbon and oxygen stable isotope measurements were performed on sixty whole rock powdered samples distributed throughout the studied succession in the IsoTOPIK Laboratory at the University of Burgos (Spain) Scientific and Technology Centre. Analyses were performed using a Thermo Scientific Delta V Plus continuous flow – isotope ratio mass spectrometer (IRMS) equipped with a Gas-Bench II carbonate sample preparation and inlet system. Carbonate powder samples were digested in He-flushed borosilicate exetainers at 70 °C using water-free 99.9% phosphoric acid. To assess the accuracy (external analytical precision) and to calibrate the obtained isotopic values, the results were measured against IAEA-603 ($\delta^{13}C = +2.46‰$, $\delta^{18}O = -2.37‰$) and NBS18 ($\delta^{13}C = -5.014‰$, $\delta^{18}O = -23.2‰$) international reference materials. Results are expressed as parts per thousand with respect to the Vienna Pee Dee Belemnite standard (‰ V-PDB). The average 1 sigma internal precision error is 0.03‰ for $\delta^{18}O$ and 0.03‰ for $\delta^{13}C$. According to the reference material analyses, stable carbon and oxygen isotope values were measured accurate to the nearest 0.02‰ and 0.02‰, respectively. Reproducibility was checked by duplicate analysis of some samples, and in the case of seemingly aberrant initial results, repeat sampling and analysis was undertaken.

4. Results

4.1. Stratigraphy and sedimentology

The base of the Berroya subsection is located at the Areta River, ca. 2.1 km to the east of Nardués-Andurra village (Fig. 2). The subsection is comprised of three distinctive lithostratigraphic intervals (Fig. 2). The lowermost one (48 m-thick) consist of grey marls with some occasional sandstone beds. Sandstones are medium to fine-grained, have a tabular geometry and display a thickness ranging typically between 30 and 80 cm. Grey marls form dm- to m-thick intervals with a massive appearance that is often interrupted by thin (<30 cm) calcareous marly beds that are slightly lighter in colour (Fig. 3a). The second interval (52 m-thick) corresponds to a sequence of grain-supported breccias with large (up to several m) limestone and sandstone clasts embedded within a conglomeratic matrix, that grade upwards into laminated calcarenites with disperse, smaller (<2 cm) clasts (Fig. 3b). The upper part of the Berroya column (46 m-thick) is similar to its basal interval, with the main difference that turbidite sandstones are significantly thinner (typically 2-8 cm).

The base of the Nardués-Andurra subsection is located 0.9 km north of the homonymous village, about 2 km to the WNW following the along-strike trace of the megabreccia identified in the Berroya subsection (Fig. 2). The subsection begins just atop the uppermost distinctive calcarenite member of the megabreccia, and can be subdivided into four distinct lithostratigraphic intervals. The basal one includes a ca. 350 m-thick succession that is essentially identical to its lateral counterpart, the third interval of the Berroya subsection (Fig. 3c). Thus, dm- to m-thick marl beds dominate the succession and include frequent calcareous marls and turbiditic sandstones with tabular geometries that are often arranged in clusters and show parallel lamination, unidirectional ripples, flute-marks and bioturbation traces. Most turbidite beds range between 2 and 10 cm in thickness, although they can be as thick as 20 cm in few cases and, exceptionally, up to 90 cm-thick. Some isolated marls and thin turbidites display distorted laminations that attest to small-scale synsedimentary slumping (<10 cm). The only exception is a 3 m-thick slumped interval that affects marls and interbedded turbidites at around meter 138 of the subsection.

The following interval of the subsection is represented by a 510 m-thick succession of grey-bluish marls that include subsidiary calcareous marls and thin (typically < 2 cm) turbidite sandstones (Fig. 3d). A significant feature of this interval is the presence, in its upper part, of conspicuous carbonate nodules that range typically from 10 to 100 cm in size, show an external ochre patina and often display internal concentric laminations (Fig. 2). They appear as subspherical, ellipsoidal or elongated concretions arranged following the stratification (Fig. 3e, g) or, less frequently, as smaller concretions placed perpendicular to bedding that often preserve remains of the surrounding marls at their core (Fig. 3f). In agreement with earlier mineralogical studies (Oliva-Urcia et al., 2024), XRD analyses indicate that these nodules are composed by ferroan dolomite, calcium carbonate, quartz, illite-muscovite and chlorite. These nodules are accompanied by a slight increase in the abundance of thin turbiditic sandstones.

The third interval of the Nardués-Andurra subsection is represented by about 110 m of grey-blueish marls that include frequent thin beds (<40 cm) of limolites and rare, thin (<2 cm) fine-grained sandstones (Fig. 3h). These limolites cluster in three decametric-thick (20-25 m) groups located at the base, middle and top of the interval, which confers it a distinctive appearance in the landscape. The Nardués-Andurra subsection ends with a 56 m-thick sequence of homogeneous marls that are grey-bluish in colour, show a massive appearance, and include some rare limolite beds that are typically <30 cm-thick (Fig. 3i). As with the rest of the studied marls within the succession, previous XRD analyses indicate a homogeneous composition that is dominated by quartz, calcium carbonate, illite-muscovite and chlorite (Sierra-Campos et al., 2025).

The Berroya and Nardués-Andurra subsections can be tied into a composite section (Izaga composite section, ICS) thanks to the undoubtful lateral continuity of the megabreccia that is identified at the middle part of the Berroya subsection and underlies the Nardués-Andurra subsection. Several authors have proposed different names for the stratigraphic units identified at different sectors of the Jaca-Pamplona Basin (Mutti et al., 1972; Puigdefábregas, 1975; Remacha et al., 1987, 1998; Payros, 1997; Payros et al., 1999; Oms et al., 2003; Montes, 2009; Garcés et al., 2020; Roigé et al., 2023). We have followed the updated nomenclature by Roigé et al. (2023) to name the different intervals at the ICS, since its enables identification and correlation of the different units across the entire basin. The basal 450 m of the ICS can be identified as the upper part of the Jaca Turbidites, which constitute the uppermost part of the Hecho Group (Figs. 2, 3a, 3c). This interval represents sedimentation in a deep-sea fan by distal, diluted turbidity currents (thin-bedded sandstones) and hemipelagic settling during periods of decreased detrital input (calcareous marls). The megabreccia located between m 48-100 of the composite section (Figs. 2, 3b), which we call Berroya, most likely corresponds to the youngest base-missing megabreccia identified by Payros et al. (1999) in the upper part of the Hecho Group succession about 15 km to the NW.

The next interval of the ICS (meter 450 to 950) can be assigned to the distinctive Larrés Formation (Figs. 2, 3d). This 500 m-thick unit attests to the transition undergone in the basin from an axial turbiditic trough to a shallower slope setting in which deep-water turbidites were replaced by distal prodeltaic marls (Payros et al., 1999; Labaume et al., 2016; Roigé et al., 2023). The upper part of the Larrés Formation, between meters 770 and 930, includes ferroan dolomitic concretions that have been identified at the same stratigraphic position across the Jaca-Pamplona Basin (Figs. 2, 3e, 3f, 3g) (Remacha and Picart, 1991; Martí Bono and Plana, 1996; Boya, 2018; Oliva-Urcia et al., 2024). The magnetic, petrographic and geochemical properties of these concretions indicate that they formed by dolomitic cementation of surrounding marls in the methanogenesis zone during the early diagenesis (<200 m of burial), a mechanism that demands large amounts of organic matter in order to drive diagenetic reactions beyond the stage of depleting dissolved seawater sulphate (Larrasoaña et al., 2007; Roberts et al., 2011; Oliva-Urcia et al., 2024).

The next interval of the ICS (meter 950 to 1060) corresponds to the so-called Urroz limolites (Figs. 2, 3h), which have been classically considered as the lateral counterpart to the west of the deltaic sandstones of the Sabiñánigo sandstone (Puigdefábregas, 1975; Garcés et al., 2020). The uppermost interval recorded in the ICS is represented by 56 m of marls attributed to the Pamplona Formation (Figs. 2, 3i) (Mangin, 1959–1960). This unit represents prodeltaic sedimentation sourced, as it is also deduced for the the Larrés and Urroz formations, from the westward-prograding deltaic system typified by the Belsué-Atarés Formation (Puigdefábregas, 1975; Garcés et al., 2020). The conspicuous presence of the deltaic Sabiñánigo sandstone between the prodeltaic marls of the Larrés and Pamplona formations has been interpreted as an isochronous progradation of the deltaic system in response to an intensified hydrological cycle driven by the Middle Eocene Climate Optimum (MECO) (Peris-Cabré et al., 2023; Lasluisa et al., 2024).

Planktonic foraminiferal faunas obtained both at the eastern (Canudo and Molina, 1988; Canudo et al., 1988; Gonzalvo, 1992, 1997) and western (Payros, 1997; Payros et al., 1999) parts of the Jaca-Pamplona Basin consistently place the Lutetian/Bartonian boundary in

Fig. 3. Illustrative pictures of the formations identified in the Izaga composite section.

the middle part of the Larrés Formation. Recent calcareous nannofossil data (González-Lanchas et al., 2019; Lasluisa et al., 2024) have confirmed the Bartonian age for the upper part of the Larrés Formation, but have yielded a Bartonian age also for its lowermost part that suggests, instead, that the Lutetian/Bartonian boundary is placed in the uppermost part of the underlying Jaca Turbidites. This is fully consistent with the occurrence of Chron C19n ~200 m below the boundary between the Larrés Formation and the Jaca Turbidites in the Aragón section (Oms et al., 2003).

4.2. Magnetostratigraphy

The average NRM of the samples is 179×10^{-6} A/m, although samples with values as low and as high as 62.7×10^{-6} and 1540.05×10^{-6} A/m, respectively, are also observed. In most of the samples it is possible to identify two stable components. A low temperature component, which is demagnetized between 100-150°C and up to 250-300°C, displays northern declinations and steep, positive inclinations in in situ coordinates; it is interpreted as a present-day field overprint, and will not be considered further. From 250-300°C, and up to 325-475°C, an additional high temperature component is identified and interpreted as the ChRM. ChRM directions have been classified as a function of their quality and paleomagnetic behaviour. With regards to their quality, we have identified four main types. Quality 1 (Q1, about 25% of the samples) directions show a linear decay upon temperatures that follows a clear trend towards the origin of the demagnetization plots (NA165-3A, Fig. 4). Quality 2 samples (Q2, about 50% of the samples) show either a less linear trend to the origin of the plots or an incomplete demagnetization linked to the growth of new magnetic minerals in the oven (NA171-2B, Fig. 4). Quality 3 (Q3, about 19% of the samples) directions are defined by a cluster that can be fitted to the origin of the demagnetization plots (NA081-1A, Fig. 4). In the remaining 6% of the studied samples (Q4), unstable directions prevented calculation of any paleomagnetic component (NA096-1A, Fig. 4). Only Q1 and Q2 ChRM directions are considered to provide reliable directions and have been used to calculate VGP latitudes and build the local sequence of polarity changes (LPS).

The ChRM identified in the studied rocks shows three main types of paleomagnetic behaviour, which are similar to those reported by previous authors in the northern fringe of the Jaca-Pamplona basin (Larrasoaña et al., 2003a, 2003b; Oms et al., 2003). In most cases, the unblocking temperature of the ChRM clearly exceeds 375°C-400°C, suggesting the dominant contribution of magnetite (Behaviour 1, e.g. NA165-3A, Fig. 4). In other cases, an additional, smaller decay in intensity below 350°C appears to signal the additional contribution of magnetic iron sulphides to the ChRM (Behaviour 2, e.g. NA171-2B, Fig. 4). When this happens, the fractions of the ChRM identified below and above 350°C tend to be subparallel (NA171-2B, Fig. 4).

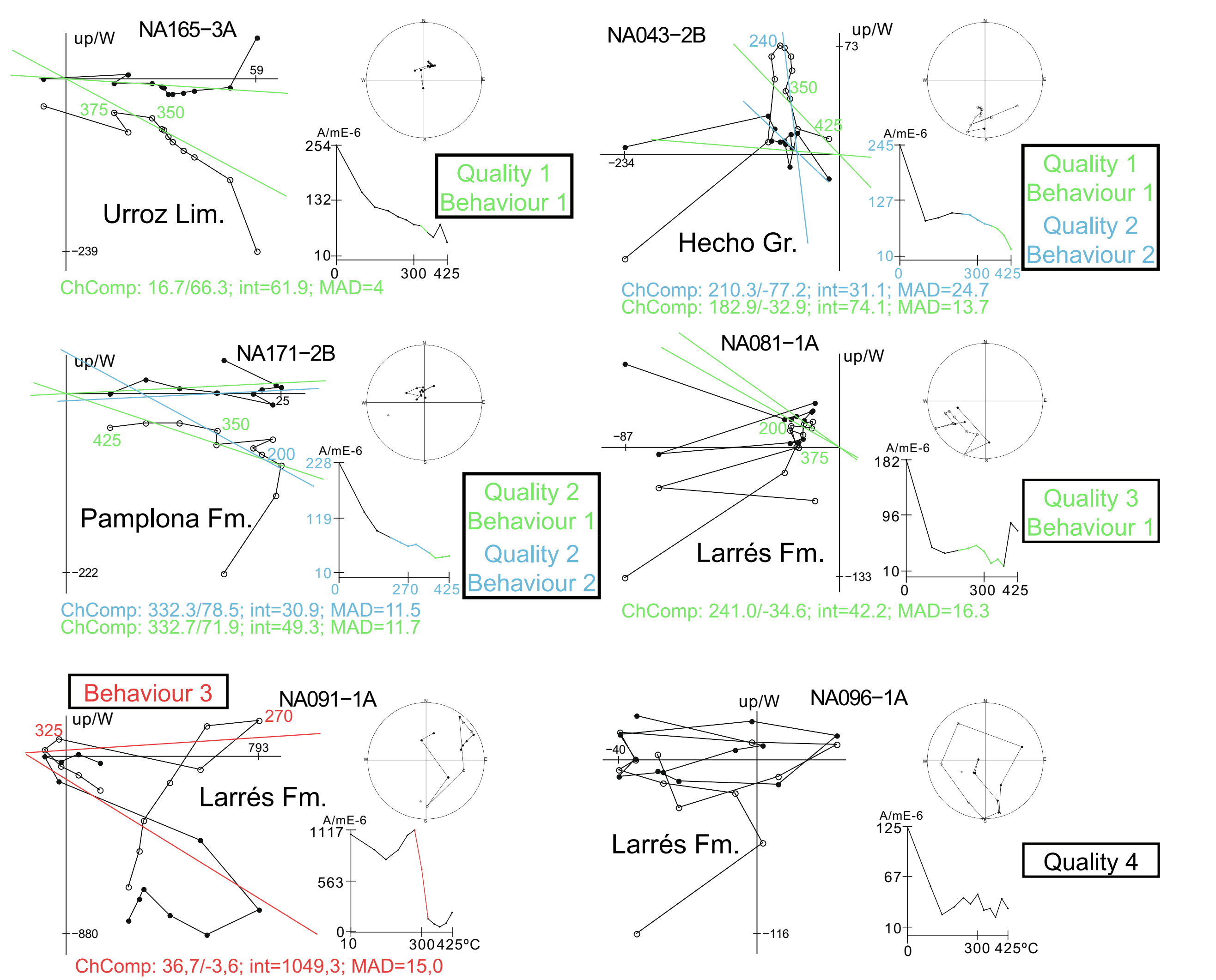

Fig. 4. Thermal demagnetization plots of some representative samples from the Izaga section after bedding correction, showing the four different qualities and the three paleomagnetic behaviours described in the text.

These ChRM directions carried by magnetite and magnetic iron sulphides in the same samples show either northerly, positive directions or southerly, negative directions after tilt correction. Although a fold test cannot be performed due to the homogeneous dipping of the succession, ChRM directions are more similar to the expected reference direction (Pedrera et al., 2023) after bedding correction (Fig. 5a) and its primary character is fully supported by several fold test carried out in the Lutetian-Bartonian rocks in the surroundings (Pueyo et al., 2002, 2025; Larrasoaña et al., 2003b, 2004; Silva-Casal et al., 2019). It is also worth noting that the means of the normal and reverse polarity ChRM directions are not fully antipodal, as evidenced by the reversal test (Fig. 5b), probably due to the partial overlap between the ChRM directions and the present-day-field component. Overall, these circumstances suggest that the ChRM in samples showing Behaviours 1 and 2 is a primary magnetization acquired during the formation, or shortly after, of the studied rocks (Fig. 5a, b).

In the last type of behaviour (Behaviour 3), the ChRM is associated with a very sharp and conspicuous decrease in the NRM intensity observed below 325°C-350°C, after which no remanence is left (NA091-1A, Fig. 4). This points to magnetic iron sulphides as the carriers of the ChRM at the expense of magnetite, which appears to be absent in these samples as it is derived from the rock magnetism analyses. These ChRM directions are typically associated with positive but somehow low (e.g., 15-60°) VGP latitudes (Fig. 6), which suggests a remagnetization process occurred when the beds were slightly tilted. Behaviour 1 accounts for about 78% of the calculated directions and is found throughout the section, although it clearly dominates in its uppermost 300 m. Behaviour 2 (ca. 8% of the directions) is observed mainly in the Jaca Turbidites and the Pamplona Formation. Behaviour 3 (8% of the directions) is found at three distinctive intervals (125-200, 290-360 and 500-650m) within the Jaca Turbidites and the Larrés Formation, broadly coinciding with parts of the section where no ChRM directions could be identified due to the low intensity and poor quality of the NRM signal (e.g., Q4 samples, 6%). To calculate the VGP and establish the LPS, only the ChRM directions carried by magnetite (Behaviours 1 and 2) are considered (Fig. 6).

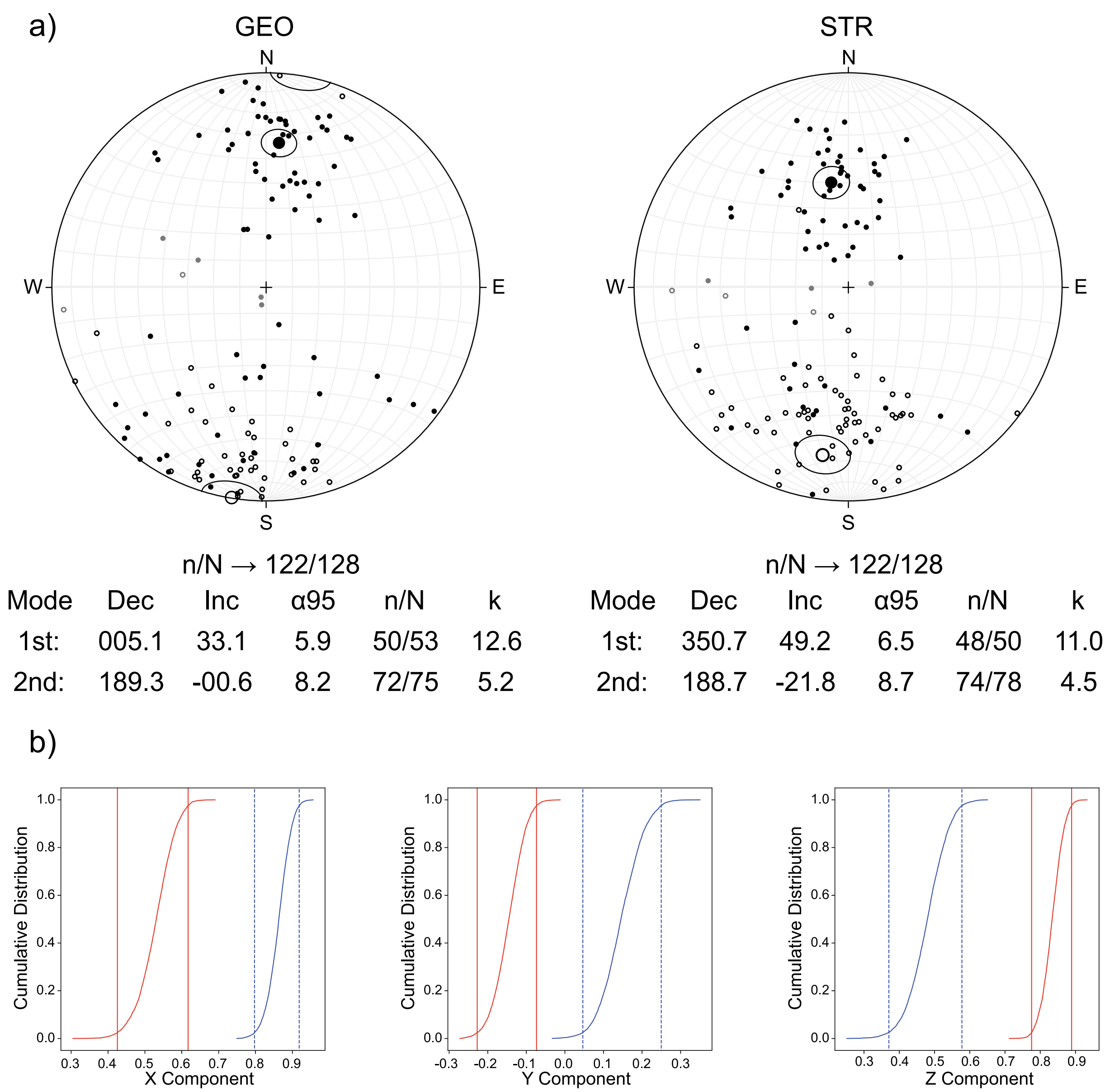

Fig. 5. a) Stereographic projection of the ChRM directions used to construct the local polarity sequence (Quality 1 and 2 ChRM directions regarded as primary in origin, Behaviours 1 and 2), shown before and after tilt correction. b) Bootstrap reversal test (Tauxe et al., 1991) showing cumulative distribution of the normal and reversed polarity directions (after tilt correction) in cartesian coordinates of the means of 1000 pseudo-samples which yield a negative result.

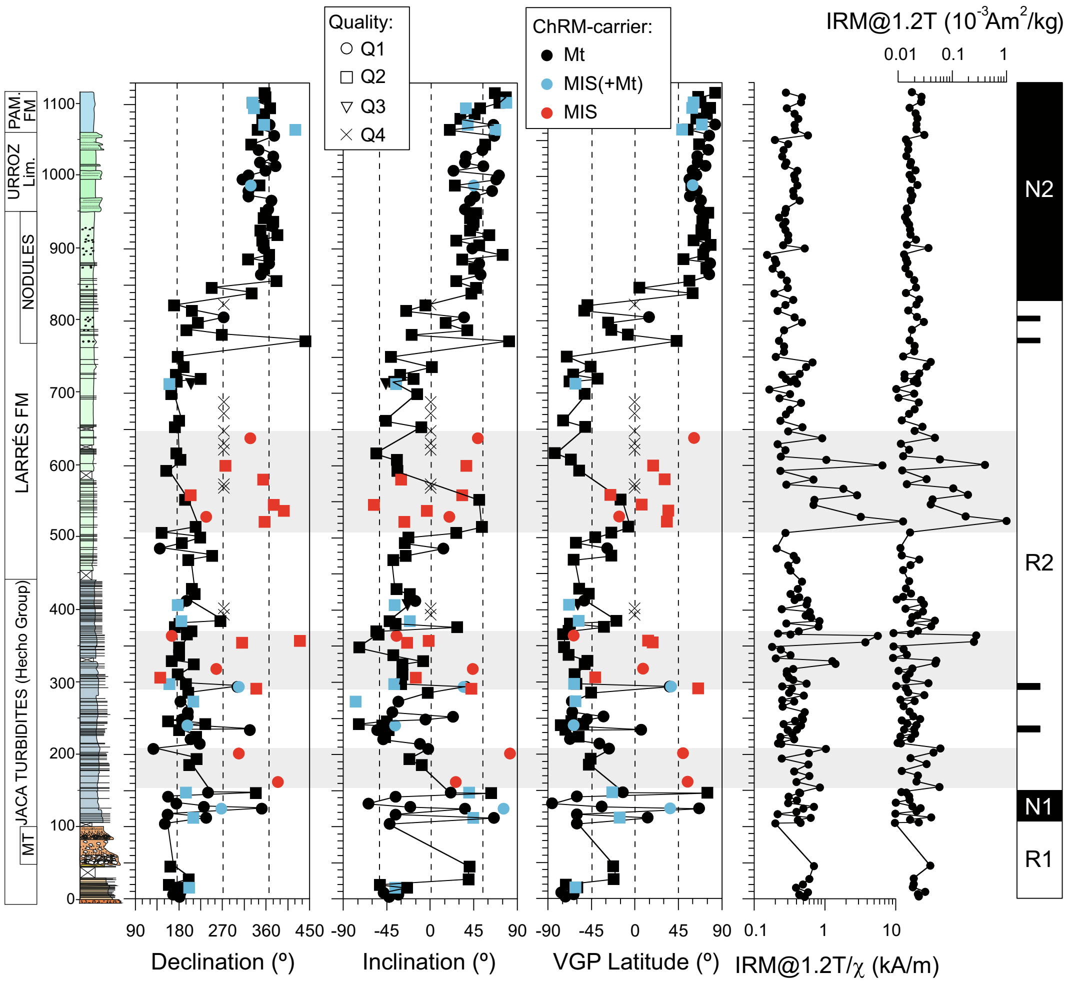

Fig. 6. Lithostratigraphy of the Izaga composite section with magnetostratigraphic results (Declination, Inclination and VGP) using quality 1 and 2 samples, and the local polarity sequence (LPS). $IRM_{1.2T}$ and the $IRM_{1.2T}/\chi$ ratio are also shown. Grey areas are the iron sulphides areas. Mt: Magnetite; MIS(+Mt): Magnetic iron sulphides + magnetite; MIS: Magnetic iron sulphides.

4.3. Rock magnetism

Of all the non-destructive magnetic properties measured and inter-parametric ratios calculated, it seems that the most valuable one is the $IRM_{1.2T}/\chi$ ratio, because it enables an initial assessment of the dominant magnetic mineralogy to be achieved (Peters and Dekkers, 2003; Larrasoaña et al., 2007; Liu et al., 2012). Values of <2 kA/m are observed through the section and corroborate the dominant presence of magnetite throughout the studied succession. It seems that the additional presence of magnetic iron sulphides suggested by paleomagnetic results of Behaviour 2 samples is not detectable by means of $IRM_{1.2T}/\chi$ ratios, which points only to their subsidiary occurrence. The intervals at 125-200, 290-360 and 500-650 m are characterized, in contrast, by larger-than-background $IRM_{1.2T}/\chi$ ratios that range between 2 and 13 kA/m, which points to a larger concentration of magnetic iron sulphides (Roberts et al., 2011) that is in consonance with the paleomagnetic results of Behaviour 3 samples. Although previous studies have reported pyrrhotite as the magnetic iron sulphide present in Eocene marls of the Jaca-Pamplona Basin (Larrasoaña et al., 2003b, 2004), the range of $IRM_{1.2T}/\chi$ ratios presented here clearly points to greigite (Larrasoaña et al., 2007; Roberts et al., 2011). The fact that $IRM_{1.2T}$ values are higher-than-background precisely at the intervals with highest $IRM_{1.2T}/\chi$ ratios clearly corroborates the somehow abnormal concentration of greigite at these positions (Fig. 6).

Thermal demagnetization of the three-composite IRM (Lowrie, 1990) corroborates the results derived from $IRM_{1.2T}/\chi$ ratios. Thus, the softest IRM component shows the highest intensities and is fully demagnetized below 600°C in the vast majority of samples, which indicates the dominance of magnetite regardless of the paleomagnetic behaviour (Fig. 7b). The slight drop in remanence observed 300°-350°C for the intermediate and hard IRM components, especially in Behaviours 2 and 3 samples, seems to confirm the additional presence of magnetic iron sulphides. We attribute to the heterogeneous occurrence of these sulphides the fact that they do not seem to dominate the IRM even in Behaviour 3 samples. Low-Temperature experiments are very similar regardless of paleomagnetic behaviour and show an exponential decay below 50K that might signal the presence of superparamagnetic and/or paramagnetic particles before diminishing more gradually up to room temperature. The lack of a shift around ~120K prevents confirmation of the presence of magnetite through it Verwey transition, probably because it is present in low amounts or is partially oxidized (see Liu et al., 2012) (Fig. 7a). Thermomagnetic runs are also very homogeneous regardless of paleomagnetic behaviour, and provide no diagnostic tool for identifying the magnetic mineralogy due to the neoformation of large amounts of magnetite upon heating at >400°C at the expense of pyrite, as it is deduced from the much more intense cooling curves and their associated increase below 580°C (Larrasoaña et al., 2003b) (Fig. 7c).

4.4. Calcareous nannofossil biostratigraphy

The autochthonous components of the ICS calcareous nannofossil

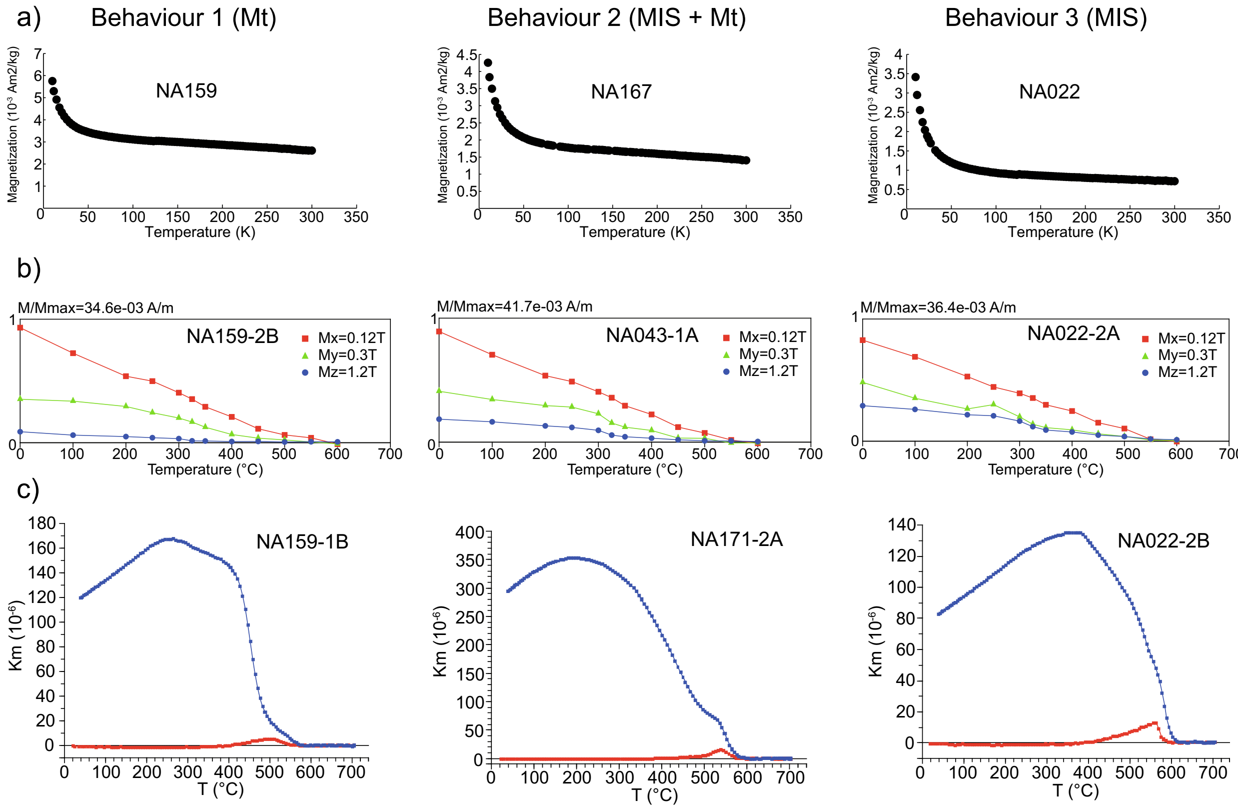

Fig. 7. Rock magnetic data for representative samples of each of the three paleomagnetic behaviours. a) Temperature-dependent magnetization between 25 and 300 K. b) Thermal demagnetization of the IRM applied in the three orthogonal axes. c) Temperature-dependent susceptibility between 25 and 700 °C.

assemblages have allowed the recognition of the most significant bioevents of the early Bartonian. The summary of recognized zones and main biohorizons is given in Fig. 8 and described in detail below. It should be noted that *Chiasmolithus solitus* is present throughout the entire section, which together with the absence of *Blackites gladius* and the sequence of biohorizons described below allows us to assign the ICS to zones NP16 of Martini (1971), CP14a of Okada and Bukry (1980), MNP16-MNP17A of Fornaciari et al. (2010), and CNE14-CNE15 of Agnini et al. (2014) (Fig. 8). In the following, the biozonations of Fornaciari et al. (2010) and Agnini et al. (2014) have been used to build the biostratigraphy of the ICS.

Reticulofenestra umbilica (>14 μm) and common *Cribrocentrum reticulatum*, the lowest occurrences of which mark the base of zones CNE13 and CNE14 respectively, are present throughout the ICS. Their presence, together with the absence of the zone CNE15 marker, *Dityococcites bisectus* (>10 μm), in the first 842 m of the section indicates that this interval corresponds to zone CNE14. The presence of *Cribrocentrum erbae* from the base of the ICS is noteworthy. According to Agnini et al. (2014), this taxon is present throughout the CNE16 zone but showing rare abundances. In the ICS, however, it appears continuously and is relatively abundant (2%) from zone CNE14 upwards.

Sphenolithus furcatolithoides A and B were introduced by Agnini et al. (2014) to differentiate two morphotypes of this species that, despite showing a similar morphology, presented a different birefringence and extinction pattern. According to these authors, the differential optical behavior of these morphotypes together with the stratigraphic distribution suggest that they are separate taxa. For nomenclature stability, these authors preferred to refer to both these morphotypes as *S. furcatolithoides*, a criterion that we have maintained here. The HCO of *Sphenolithus furcatolithoides* B is recorded at the base of the Larrés Formation at meter 441±3. However, it is continuously present up to meter 489±4, where its HO is recorded, a datum that is used to mark the boundary between subzones MNP16A and MNP16B of Fornaciari et al. (2010) (Fig. 8). The HCO and HO of *Sphenolithus furcatolithoides* B appear separated because of the expanded nature of the succession, which contrasts with other sections where sedimentation rates are much lower (e.g., Alano, Fosio, ODP Sites 1052 and 1263) and both events appear much closer to each other and, very frequently, even in the same horizons (Fornaciari et al., 2010).

Dictyococcites bisectus (>10 μm), the marker species of the base of zone CNE15 (Agnini et al., 2014) and subzone MNP16Bb (Fornaciari et al., 2010), first occurs at meter 809.5±4.5. However, from meter 769 ±4 we have registered the presence of relatively large *Dictyococcites hesslandii* (9-9.9 μm), which can be erroneously ascribed to *Dictyococcites bisectus* if an accurate measurement of each individual specimen is not carried out.

Sporadic occurrences of *Furcatolithus predistentus* have been found in the upper part of zone CNE14. These are isolated specimens in few samples and therefore cannot be taken as the true lowest occurrence of this species. We consider that the lowest occurrence (LO) refers to the lowest continuous occurrences of taxa, and it is considered that the occurrence of a taxon is continuous when it appears in a series of successive samples. We observe the true continuous occurrence of *Furcatolithus predistentus* from meter 842±4 upwards.

The LO of *Furcatolithus obtusus,* which is used to mark the boundary between subzones MNP16B and MNP17A of Fornaciari et al. (2010), is recorded at meter 1054±3 at the top of the Urroz limolites. As with *Furcatolithus predistentus*, *Furcatolithus obtusus* also appears sporadically in a stratigraphically lower sample, in this case at meter 781. As it is an isolated specimen in a single sample, it has not been taken into account when defining the LO of this species.

The HCO of *Sphenolitus spiniger* at Izaga section has been recorded at meter 1099±4, about 40 m above the base of the Pamplona Formation.

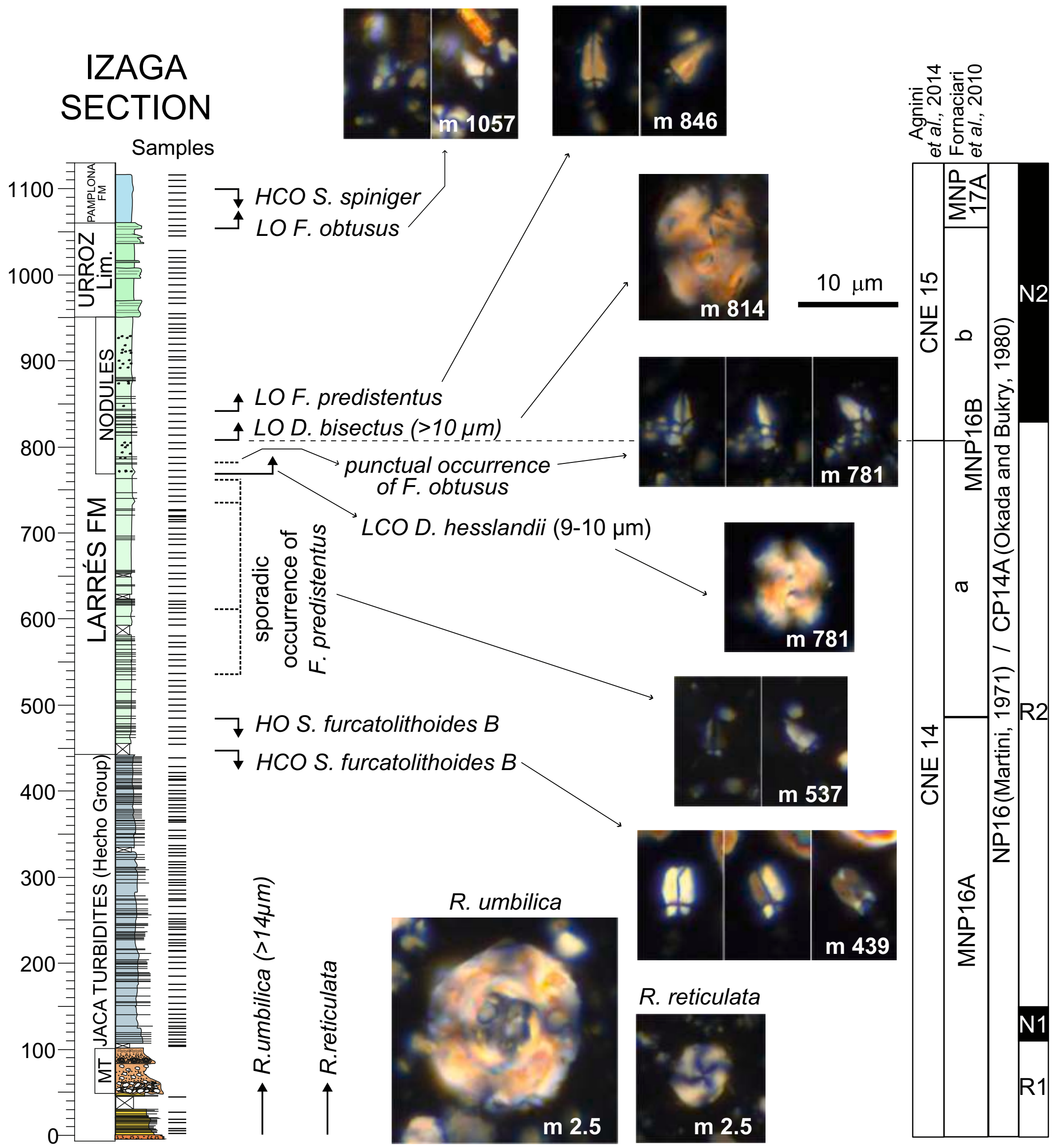

Fig. 8. Location of the main calcareous nannofossil events recognized across the Izaga section. Zones in columns are following Agnini et al. (2014), Fornaciari et al. (2010). Light Microscope (LM) images of selected calcareous nannofossil taxa at their highest or lowest occurrence levels. All photos are in cross-polarized light.

4.5. Calcareous nannofossil assemblages

The calcareous nannofossil assemblages are mainly dominated by placoliths, which represent an average of 82% of the recorded autochthonous calcareous nannofossils. Among placoliths *Coccolithus*, *Cribrocentrum*, *Cyclicargolithus, Dictyococcites* and *Reticulofenestra* are the most abundant taxa. *Sphenolithus*, *Zygrhablithus*, *Lanthernithus*, *Discoaster* and braarudosphaerids are the secondary components of the calcareous nannofossil assemblages but each of them never exceeds 12%. The rest of the principal components of the calcareous nannofossil assemblages are *Helicosphaera*, *Pontosphaera*, *Neococcolithes Clausicoccus* and *Chiasmolithus*, which never exceed 5% individually.

The calcareous nannofossil assemblages, however, show significant changes throughout the ICS especially in a stratigraphic interval, referred to as the disturbance zone, located in the upper part of the Larrés Formation, between meters 640 and 930, where we observe a fall in the total abundance of calcareous nannofossils and the increase in reworked species (Fig. 9). The smaller representatives of the Noelaerhabdaceae family (*Reticulophenestra minuta* and specimens smaller than 5 µm of *Reticulofenestra dictyoda*, *Dictyococcites hesslandii* and *Cyclicargolithus floridanus*; subsequently referred to as small reticulofenestrids) show similar trends but opposite to those of the larger reticulofenestrids (*R. dictyoda* and *D. hesslandii* larger than 5 µm, *Reticulofenestra umbilica, Dictyococcites bisectus, Cribrocentrum reticulatum* and *Cribrocentrum erbae*). The small reticulofenestrids represent around 40% of the association in most of the studied samples. However, these mean values are broadly exceeded in the disturbance zone between meters 640 and 930. This increase in small reticulofenestrids is abrupt, peaking in the interval between meters 650 and 725, where they occasionally exceed 80% of the autochthonous assemblages. The trend of large reticulofenestrids is the opposite of that shown by the small reticulofenestrids. The increasing relative abundance trend recorded by the large reticulofenestrids throughout the succession (from 10% to 30%) is interrupted by a pronounced relative abundance decrease in the disturbance zone between meters 640 and 930 (Fig. 9).

The genus *Coccolithus,* which in the ICS is mainly represented by *C. pelagicus* and *C. formosus* and in a lesser extent by *C. eopelagicus*, shows smaller magnitude changes in relative abundance. It should be noted that the minimum values for both *C. pelagicus* and *C. formosus* have been recorded in the disturbance zone of the upper part of the Larrés

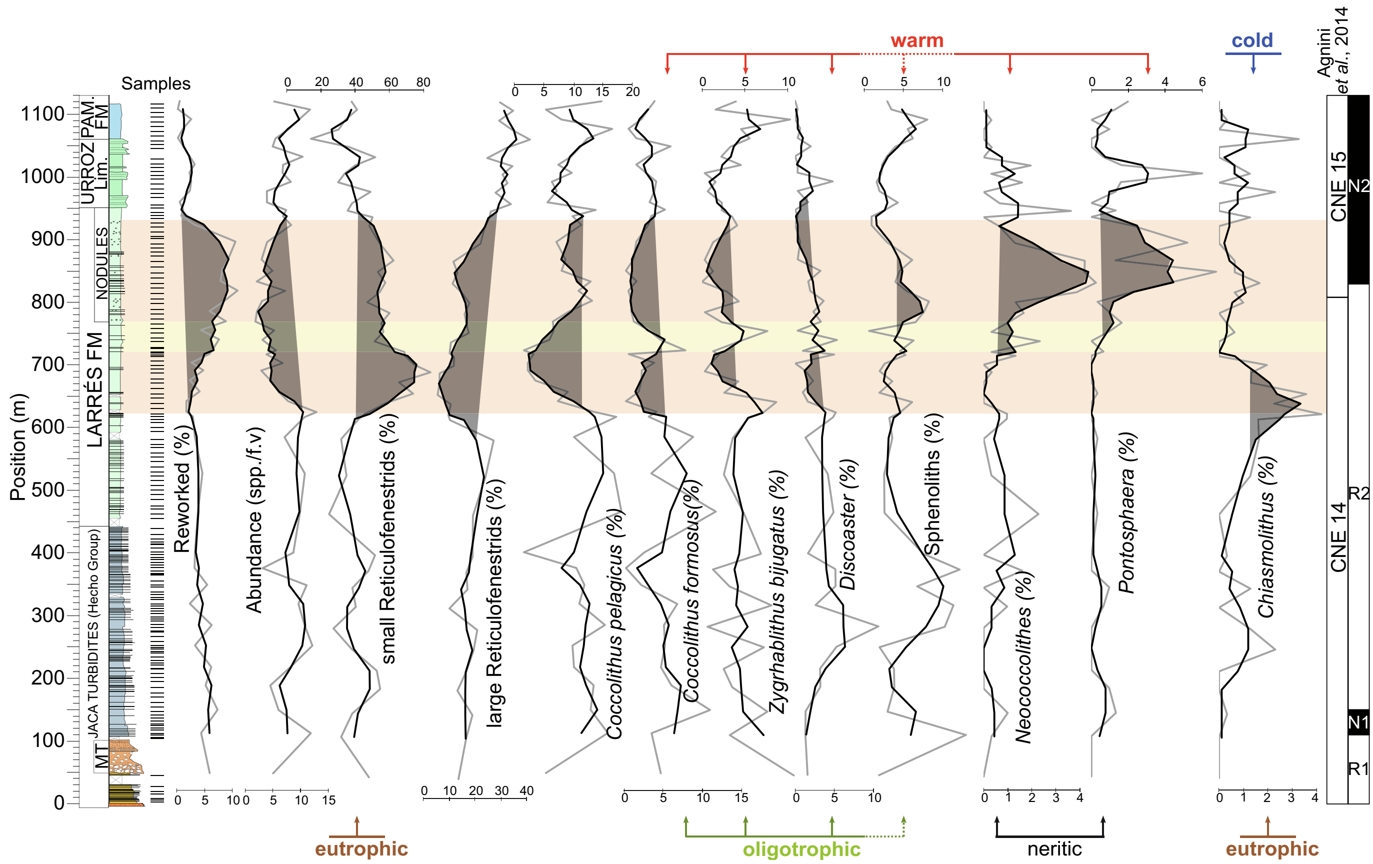

Fig. 9. Calcareous nannofossil assemblage variations throughout the Izaga section, including the relative abundance of reworked forms, the autochthonous calcareous nannofossil total abundance expressed in observed specimens per FOV (field of view) and the relative abundance of selected, environmentally significant autochthonous taxa (see supplementary material for quantitative data). The thick black curves show 3-point running mean values and illustrate general trends. Note that scale bars are different in each case. The main ecological preferences are also indicated (see supplementary material). Light orange shading indicates the lower and upper parts of the disturbance zone, whereas light yellow shading marks the intervening interval described in the text.

Formation, coinciding with the interval where the main changes in calcareous nannofossil assemblages take place (Fig. 9). Other taxa, such as *Zygrhablithus bijugatus* and in lesser extent *Discoaster*, also recorded their minimum relative abundance values in the disturbance zone. The sphenoliths, mainly represented by the species *S. furcatolithoides*, *S. moriformis* and *S. spiniger*, show highly fluctuating values throughout the section. *Postosphaera* and *Neococcolithes* are very scarce throughout the Jaca turbidites and the lower part of the Larrés Formation. However, they show two abundance peaks, the first in the Larrés Formation, in connection with the interval with the highest percentage of reworked species, in the upper part of the disturbance zone, and the second in the middle part of the Urroz limolites, where a slight increase of the reworked species is also recorded.

4.6. Carbonate carbon and oxygen stable isotopes

At the ICS, δ^{18}O values are characterized by very negative values between -3.5 to -6‰ that might signal an important diagenetic overprint. Most of the variability concentrates in the lower parts of the succession and the disturbance zone, respectively. The running average indicates just rather constant δ^{18}O values throughout the succession, with a faint shift to lighter δ^{18}O values within the disturbance zone and around the R2/N2 boundary that is just below the average value of -4.7‰. δ^{13}C values range from -1.5 to 0.6‰ and display and average of -0.6‰ (Fig. 10) that is more similar to what is reported in most sections elsewhere (see Giorgioni et al., 2019), likely in response to a higher stability against diagenetic overprints. Although individual δ^{13}C values are somehow scattered, especially in the lower half of the succession, the running average provides a consistent view on the main variations observed within the section. Thus, it indicates relatively heavier values in the lower part of the section that show a progressive trend to lighter values upwards from 300 m. Distinctively, the lightest values are observed within the disturbance zone between 620 and 930 meters, thereby encompassing the uppermost and lowermost parts of R2 and N2, respectively (Fig. 10). This shift is followed by a trend to heavier values within N2 that extends towards the top of the section. The trends observed in our section are comparable to those in the Belsué and Yebra de Basa sections located about 80 km to the SE, where slight shifts to lighter δ^{13}C and δ^{18}O signals have been also reported around a transition from reverse to normal polarities placed at a similar stratigraphic position (uppermost part of the Larrés Formation, Peris-Cabré et al., 2023). This indicates a consistent response of the South Pyrenean basin to the palaeoenvironmental changes undergone during deposition of the disturbance zone.

5. Discussion

5.1. Magnetobiochronology of the Izaga composite section

The combination of paleo- and rock magnetic results indicates that magnetite is the dominant magnetic mineral in the studied succession, and that it records a primary magnetization acquired at or shortly after deposition (Behaviours 1 and 2). Given the turbiditic and prodeltaic origin of the studied sediments, a detrital origin for magnetite is considered as the most likely in agreement with previous authors (Oms et al., 2003; Larrasoaña et al., 2003b). Minor amounts of greigite present

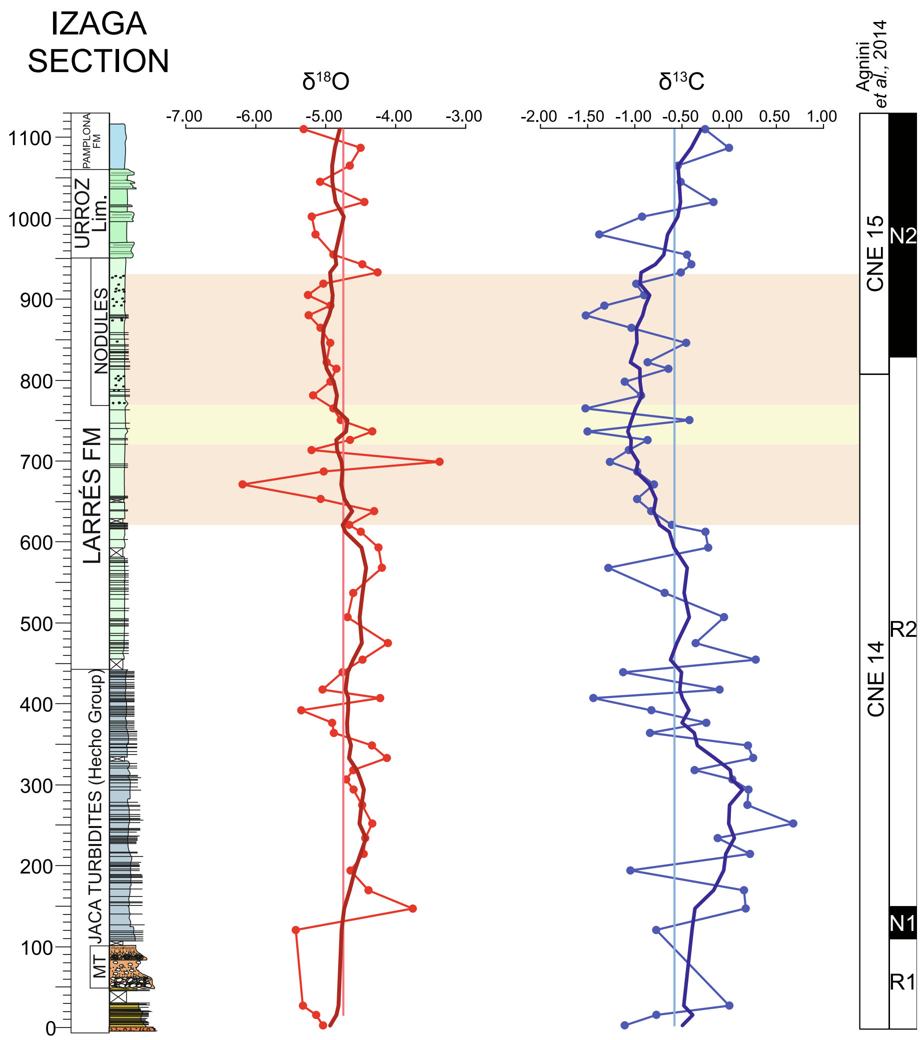

Fig. 10. Depth variations of $\delta^{18}O$ and $\delta^{13}C$ values of the ICS shown along its stratigraphic log and local polarity sequence. Stable isotope values for individual samples are shown along with a 9-sample running-average (thick-dark line) and the average value for each stable isotope (light line). Disturbance zone is also shown in orange and yellow shading.

in Behaviour 2 samples appear to carry also a remanence that is subparallel to that carried by magnetite. In the context of the studied succession, we interpret that this greigite formed authigenically shortly after deposition of the sediments, as a result of an incomplete pyritization process that occurred during the early diagenetic degradation of organic matter and the establishment of reductive conditions (Larrasoaña et al., 2007; Roberts et al., 2011). Such reductive conditions were likely not too strong in order to enable the preservation of detrital magnetite particles carrying a stable primary remanence. As opposed to this, larger amounts of greigite in Behaviour 3 samples appear to be associated to erratic ChRM directions, to the absence of paleomagnetic directions carried by magnetite, and to the identification of relatively lower amounts of magnetite in rock-magnetic experiments. We interpret this as the result of authigenic growth of greigite at a later diagenetic stage at which only coarser magnetite grains survived reductive dissolution. Given the presence of methane-derived, ferroan dolomitic concretions in the upper part of the Larrés Formation (Oliva-Urcia et al., 2024), we interpret that greigite in Behaviour 3 samples formed below the sulphate-reduction zone in response to the more severe reductive conditions, as has been reported in other marine sediments (Larrasoaña et al., 2007; van Dongen et al., 2007).

In light of these results, and for the sake of consistency through the studied succession, we have constructed the local polarity sequence of the (ICS) using ChRM directions that are carried by magnetite in Behaviour 1 and 2 samples that display only quality types Q1 and Q2 (66% of the directions). The criteria used to define a magnetozone is that it is delineated by at least two consecutive sites with the same polarity; single site magnetozones are not considered reliable and are represented as half-width bars in the LPS. We have defined an upper normal magnetozone, labelled N2, that spans the uppermost 286 m of the ICS (Fig. 6). The rest of the succession is dominated by reverse polarity directions with the exception of some single-site levels that are located just below N2 and scattered within the Jaca Turbidites. The two single-sites located below N2 can be readily interpreted as slightly delayed remanences occurred in the upper part of the underlying reverse interval. Concerning the single-site normal-polarity intervals at the base of the Jaca Turbidites (110-150 m interval), a striking feature is the conspicuous clustering of three of them within a 40 m-thick interval located just above the Berroya megabreccia (Fig. 6). Given their position, it is highly unlikely that they represent slightly delayed remanences comparable to those found just below N2. Instead, they appear to be located at a stratigraphic position equivalent to that of Chron C19n in the neighbouring Aragón section (Oms et al., 2003). If so, this interval can be regarded as a poorly preserved, normal polarity chron that we tentatively label as N1 and that splits the long interval of reverse polarity directions into two parts, R1 and R2 (Fig. 6).

Whatever the case, correlating the sequence of polarity changes of the ICS to the updated Geomagnetic Polarity Time Scale of 2020 (GPTS

2020, Speijer et al., 2020) is straightforward in light of the nannofossil results. Thus, the first appearance of *Dictyococcites bisectus* (>10 μm) in the uppermost part of R2, which marks the boundary between CNE14 and CNE15 (Agnini et al., 2014) near the top of Chron C18r, enables the correlation of R2 and N2 with chrons C18r and C18n.2n, respectively (Fig. 11). In the upper part of the studied succession, the lack of reverse directions within the lowermost part of the Pamplona Formation indicates that the studied record does not reach Subchron C18n.1r, which constrains the top of the section to be older than 39.666 Ma (GPTS 2020, Speijer et al., 2020). This is consistent, keeping in mind errors associated with biostratigraphic data (Messaoud et al., 2021), with the identification of the HCO of *Sphenolithus spiniger* in the upper part of C18n.2n. In the lower part of the ICS, the identification of the purported normal polarity interval N1 as Chron C19n is rather feasible, because it results in broadly homogeneous sedimentation rates for the whole succession of around 68 cm/kyr, which are consistent, albeit a bit higher, with those reported by Oms et al. (2003) for the same interval of the Aragón section (~63 cm/kyr). Such accumulation rates were only interrupted by the geologically instantaneous deposition of the Berroya megabreccia and by somehow reduced sedimentation rates between the first appearance of *Dictyococcites bisectus* (>10 μm) and the base of Chron C18n.2n. In this regard, however, it is worth noting that only very accurate measurements have enabled the differentiation between *Dictyococcites bisectus* (>10 μm) and relatively large specimens (9-9.9 μm) of *Dictyococcites hesslandii*; the misidentification of the former species by the latter might result in a slightly older apparition *Dictyococcites bisectus*, smoothing the sedimentation rates across the studied succession (Fig. 11). The correlation of N1 with C19n is fully supported by the identification of the highest occurrence of *Sphenolithus furcatolithoides* B within the middle part of R2, because this event has been widely reported within the middle part of C18r in different land-based sections (e.g., Alano, Bottaccione, Contessa, Massignano, Souar; Jovane et al., 2006, Jovane et al., 2007, Jovane et al., 2010; Fornaciari et al., 2010; Agnini et al., 2011; Messaoud et al., 2021; Coccioni et al., 2022) and deep-sea sediment cores (e.g., ODP Sites 1050-1052, ICDP Sites 1331-1334; Fornaciari et al., 2010; Bown and Dunkley Jones, 2012; Agnini et al., 2014) worldwide, including the neighbouring Aragón section (González-Lanchas et al., 2019). In the southern part of the Jaca-Pamplona Basin, chron C19n has been located in different magnetostratigraphic sections along the External Sierras at the very top of the Guara Limestones Formation, which represents the lateral counterpart of the Jaca Turbidites in shallow water facies (Rodriguez-Pintó et al., 2012; Silva-Casal et al., 2019).

The resulting age model for the ICS indicates, therefore, that the section spans from the uppermost part of C19r (ca. 41.3 Ma) in the latest Lutetian to the uppermost part of Chron C18n.2n (ca. 39.7 Ma) in the middle part of the Bartonian. This age model constrains the emplacement of the Berroya megabreccia to the latest Lutetian (ca. 41.1 Ma), and hence indicates that the causes for SPECM emplacement (i.e, the rapid oversteepening and collapse of the southern margin of the basin in response to enhanced tectonic activity of the Lakora-Larra-Monte Perdido thrust systems) persisted till the latest Lutetian. It is also worth

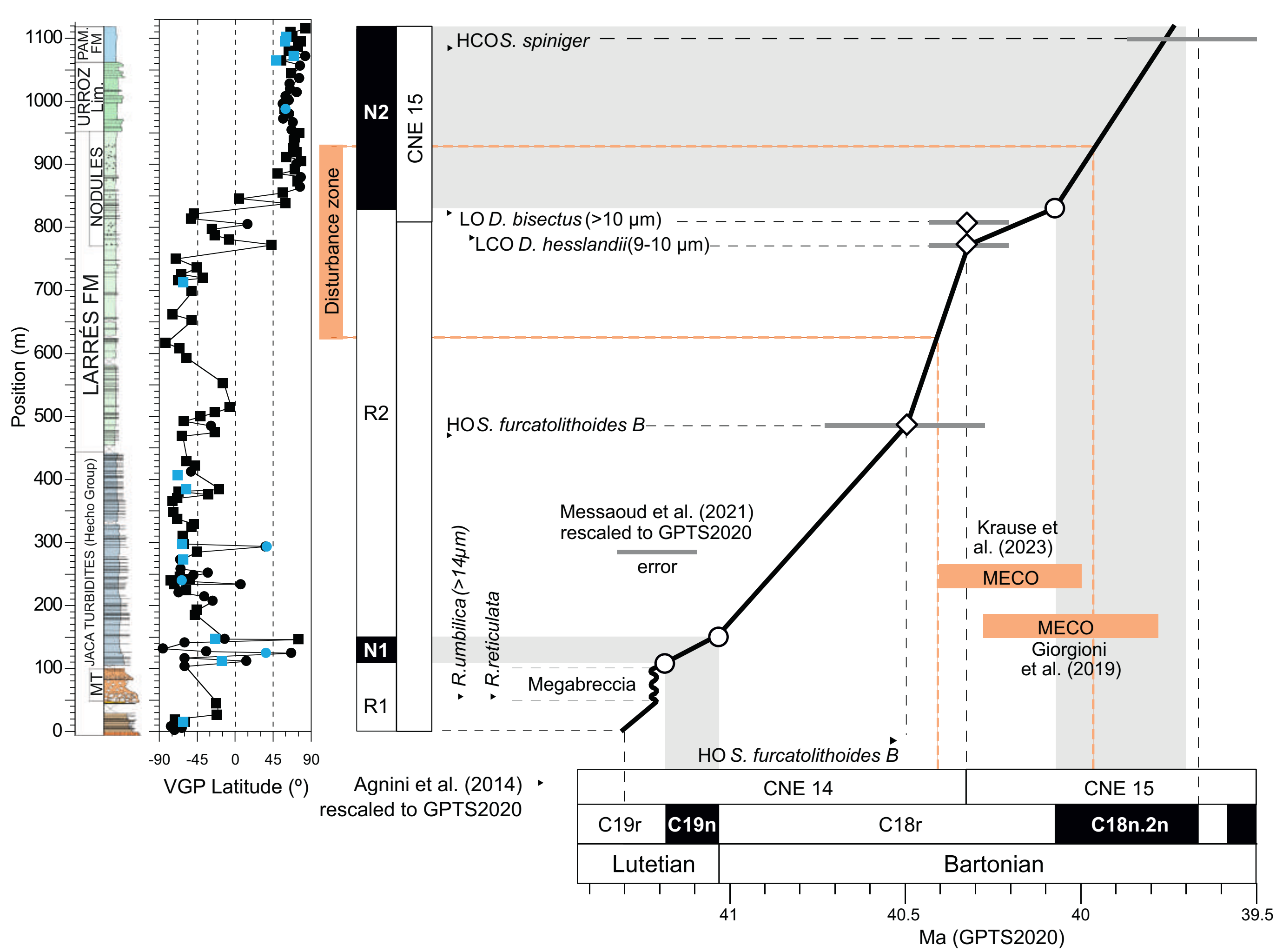

Fig. 11. Correlation of the Local Polarity Sequence (LPS) with the Global Polarity Time Scale 2020 (Speijer et al., 2020). Location of the main calcareous nannofossil events and the MECO are also shown.

noting that the resulting age model for the ICS yields an average temporal resolution of ~9 kyr and ~32 kyr for the biostratigraphic and palaeoenvironmental data, respectively, which is considered to be high enough to provide reliable results.

5.2. Implications for the Bartonian GSSP

Our results strongly suggest that the ICS includes Chron C19n, but its record appears to be incomplete and, hence, of insufficient quality to represent a significant improvement with respect to other sections that have been previously proposed to host the Bartonian GSSP. In this regard, our results concur with those of Oms et al. (2003) in portraying a Chron C19n that is not only poorly recorded by alternating normal and reverse polarity sites, but also spans a stratigraphic interval apparently shorter than its duration might demand. Thus, Chron C19n spans around 40 m at both the Izaga and Aragón sections, which according to its duration (e.g., 150 kyr, Speijer et al., 2020) yields mean accumulation rates of around 27 cm/kyr, considerably lower than that of the hosting sedimentary sequence (63-68 cm/kyr). These circumstances suggest, as already indicated by Oms et al. (2003), that the occurrence of short delays in the lock in of the magnetization carried by magnetite during the long, reverse polarity Chron C18r resulted in the partial erasure and blurring of Chron C19n. It is important to recall that problems with delayed remanences have also compromised the record of Chron C19n at most prospective sections of Botaccione and Oyambre (Payros et al., 2015a; Coccioni et al., 2022), the inaccessible Contessa Highway section being a remarkable exception (Jovane et al., 2007, 2010). Keeping in mind the very short duration of Chron C19n and the common occurrence of delayed remanences in marine sequences, we anticipate severe difficulties in finding a land-section where Chron C19n can be resolved at a resolution high enough to be used as marker of the Bartonian GSSP. The record of the short Chron C19n is often elusive also in deep-sea sediment cores. Thus, either incomplete or poor records have been reported at ODP Sites 1050 and 1052 (Ogg and Bardot, 2001), 1090 (Channell et al., 2003), and 1263 (Zachos et al., 2004). Of those sites where Chron C19n has been reliably recorded (ODP/IODP Sites 1051, Edgar et al., 2010; 1260, Westerhold and Röhl, 2013; U1331 and 1333, Pälike et al., 2010; U1403 and U1410, Norris et al., 2014), usually spanning a stratigraphic interval of 2 to 5 m, nannofossil biostratigraphic data are available only for Sites 1051 (Agnini et al., 2014), U1333 (Toffanin et al., 2013) and U1410 (Norris et al., 2014). Noticeably, the HO of *Sphenolithus furcatolithoides* B is always reported towards the middle part of C18r in these three cases.

Our results from the ICS validate the consistent identification of the HO of *Sphenolithus furcatolithoides* B within the middle part of Chron C18r (Jovane et al., 2007, 2010; Fornaciari et al., 2010; Bown and Dunkley Jones, 2012; Toffanin et al., 2013; Norris et al., 2014; Agnini et al., 2014; Messaoud et al., 2021; Coccioni et al., 2022),relatively close to the top of Chron C19n and at a chronostratigraphic position very similar to the base of the Bartonian (*Nummulites prestwichianus* level) as originally proposed in its type area of the Hampshire Basin (Dawber et al., 2011; Hooker and King, 2019). This reinforces the view that the HO of *Sphenolithus furcatolithoides* B represents one of the most suitable biostratigraphic alternatives to mark, or approach, the base of the Bartonian Stage (Payros et al., 2015a). In this regard, the expanded nature of the Izaga section, along with its superb outcrop and access conditions, place it as one of the best prospective successions to host the Bartonian GSSP.

5.3. Palaeoenvironmental inferences based on calcareous nannofossil assemblages

The high relative abundances of species prone to dissolution, such as *Zygrhablithus bijugatus* and *Reticulofenestra minuta*, as well as the scarcity of dissolution-resistant taxa, such as *Discoaster*, throughout the studied succession, show that the incipient dissolution observed in the studied nannofossil assemblages of the ICS has not significantly modified their original composition. Therefore, we regard the reported variations in the assemblages of autochthonous taxa as original and valid to interpret the palaeoecological changes occurred during the deposition of the sedimentary succession.

The most important changes observed in the calcareous nannofossil assemblages throughout the studied succession enable, keeping in mind the ecological preferences attributed to each taxon or group of taxa in this work (see Supplementary Material), to reconstruct the palaeoenvironmental shifts recorded across the disturbance zone (Fig. 9). At the beginning of this zone, between meters 640 and 720, the drop in the total abundance of calcareous nannofossils and the increase in the smaller reticulophenestrids (which occasionally exceed 82% of the assemblage) are observed simultaneously to a slight decline of warm and oligotrophic taxa, such as *Discoaster*, *Coccolithus formosus* and *Zygrhablitus* and to an increase of the cold and eutrophic specimens of the genus *Chiasmolithus*. The increase and dominance of r-strategist small reticulofenestrids in this interval suggests increased nutrient supply and eutrophic conditions. The near absence of nearshore taxa such as *Pontosphaera* and *Neococcolithes* and the increase in cool water *Chiasmolithus* suggest an increased nutrient supply due to enhanced upwelling.

After a short interval between meters 720 and 770, in which the aforementioned trends are slightly reversed, another pulse occurs in the upper part of the disturbance zone, between meters 770 and 930. The total abundance of calcareous nannofossils remains low and the small reticulofenestrids continue to be the dominant component of the assemblages. However, the most significant changes recorded in this interval are: (1) a significant increase in reworked calcareous nannofossils, which reach their maximum value between meters 800 and 870, where they represent more than 10% of the total calcareous nannofossil assemblage; (2) a new decline in oligotrophic taxa *Discoaster*, *Coccolithus formosus* and *Zygrhablitus* after a slight recovery; (3) the near absence of *Chiasmolithus*; and (4) an increase in the near shore taxa *Pontosphaera* and *Neococcolithus*. These observations suggest that the upper part of the disturbance zone was still under high nutrient supply and eutrophic conditions. However, contrary to what was occurring in the lower part of the disturbance zone, the increase in reworked species and the presence of nearshore taxa suggest that the increased supply of nutrients was likely due to continental input.

Noteworthy is the presence, between meters 821 and 850, of a very narrow variant of *Neococcolithes minutus*, being a transient aberrant form of this taxon. The holotype of *Neococcolithes minutus* (Perch-Nielsen, 1971) is a narrowly elliptical murolith with pointed ends, H-shaped cross bars and a length/width ratio of 2. The transient aberrant forms found at the ICS show a length/width ratio greater than 4, being the width of the central area less than a 1μm. These aberrant *Neococcolithes minutus* are reminiscent of the aberrant *Discoaster* species found in relation to the Paleocene-Eocene Thermal Maximum (PETM) (Bybell and Self-Trail, 1995; Aubry, 1998). Bralower and Self-Trail (2016) proposed that this transient *Discoaster* represents malformed ecophenotypes that calcified in a deep photic zone refuge during the height of the PETM due to unusually high rates of organic matter remineralization at these depths. We interpret that similar conditions associated with mineralization of organic matter in the ICS, led to the malformation of *Neococcolithes* in a similar manner to that in which the malformation of the *Discoaster* occurred during the PETM. A final aspect worth noting concerning the upper part of the disturbance zone is its striking coincidence with the occurrence of ferroan dolomite concretions of methanogenic origin, which implies degradation of large amounts of organic matter in the deep-sea environments of the Jaca-Pamplona Basin (Fig. 9) likely in response to increased fluxes of continental runoff (Oliva-Urcia et al., 2024).

5.4. Implications for unravelling palaeoenvironmental changes across the MECO

Calcareous nannofossil data from the lower part of the disturbance zone (meters 640 to 720) indicate eutrophic conditions and an associated increase in the supply of nutrients that was likely driven by a period of enhanced upwelling or changing local marine currents. After a transient (meters 720 to 750) shift to background conditions, the upper part of the disturbance zone (meters 770 to 930) records the return of eutrophic conditions and an increase in the supply of nutrients in response to enhanced runoff from the continent. Such conditions are fully supported by the methane-driven formation of ferroan dolomite concretions within the upper part of the disturbance zone (Fig. 9), since their formation has been linked to a substantial increase in the supply of labile organic matter derived from the continent (Oliva-Urcia et al., 2024). As proposed for different Eocene hyperthermal events and the Early Eocene Climate Optimum, we interpret that enhanced runoff during the disturbance zone can be related to an intensified hydrological cycle and a concomitant increase in weathering conditions and sediment production on land (Schmitz and Pujalte, 2003; Sluijs et al., 2009; Toffanin et al., 2011; Payros et al., 2015b; Intxauspe-Zubiaurre et al., 2018; D'Onofrio et al., 2021; Gandolfi et al., 2023, 2025).

The chronostratigraphic position of the disturbance zone and the ferroan dolomitic concretions, spanning the boundary between calcareous nannofossil zones CNE14/CNE15 and chrons C18r/C18n.2n, along with their palaeoenvironmental significance, clearly point to what we interpret as one of the most expanded (e.g., 290 m) records of the Middle Eocene Climatic Optimum (MECO) worldwide. The association between the disturbance zone and the MECO is further supported by the shift to lighter $\delta^{13}C$ and $\delta^{18}O$ values in calcite observed precisely within the disturbance zone (Fig. 10). In the case of $\delta^{18}O$ values, the shift to lighter values is minimal probably due to the imprint of diagenetic effects, yet it is consistent with the trend towards warmer conditions that characterizes the MECO worldwide (e.g., Jovane et al., 2007; Giorgioni et al., 2019; Krause et al., 2023). Concerning $\delta^{13}C$, the shift towards lighter values differs from other records worldwide, which, in any case, do not show a common response to the carbon cycle perturbations associated with the warming event (Giorgioni et al., 2019). In the ICS, the most negative $\delta^{13}C$ values observed throughout the disturbance zone might have been driven by the enhanced arrival of ^{12}C-richer waters of continental origin or by an increase in the degradation of organic matter (Giorgioni et al., 2019). Both processes might have been operating at the ICS during the MECO, as indicated by the presence of the ferroan dolomitic concretions within the disturbance zone in response increased continental runoff and input of labile organic matter (Oliva-Urcia et al., 2024). As also happens in other Neo-Tethyan successions (Toffanin et al., 2011; Giorgioni et al., 2019; D'Onofrio et al., 2021; Gandolfi et al., 2023, 2025), the MECO at the ICS appears to be linked to a combination of shifts in oceanic circulation (e.g. lower part of the disturbance zone) and a concomitant shift towards wetter conditions (e.g. upper part of the disturbance zone). According to our age model (Fig. 11), the MECO at the ICS spans from ca. 40.4 to 39.95 Ma, which appears to be slightly earlier than reported in other MECO records worldwide (ca. 40.3-39.8 Ma when rescaled to GPTS 2020, see Giorgioni et al., 2019) but matches the MECO duration inferred at the southern Atlantic and the equatorial Pacific Oceans from the novel study of lithium isotopes as markers of global weathering (ca. 40.4-40 Ma, Krause et al., 2023). We attribute the slight differences in the ages attributed to the MECO to its gradual onset and termination and also to the inter-site variability of the proxies (mainly O and C isotopes) used in its delineation (see Giorgioni et al., 2019).

Whatever the case, our results from the ICS portray the sedimentary expression of the MECO in the deep environments of the SPFB, and complement what has been reported from the continental and shallow marine sectors of the basin. At the Olsón section, in the continental part of the basin towards the SSE, a period of rapid fluvial progradation represented by the amalgamation of the Olsón conglomerate sheet has been reported in response to the MECO around the C18r/C18n boundary (Vinyoles et al., 2021; Peris-Cabré et al., 2023; Sharma et al., 2024) (Fig. 12). About 40 km to the NNW, down the sedimentary routing system, the Yebra de Basa section records a coeval, rapid progradation of the deltaic deposits of the Sabiñánigo sandstone on top of the slope marls of the Larrés Formation (Peris-Cabré et al., 2023). There, the peak of the MECO is recorded around the C18r/C18n boundary by shifts to more negative $\delta^{18}O$ and $\delta^{13}C$ values, comparable to those in the ICS, observed within the Sabiñánigo sandstone. Such isotopic shifts are preceded by a period of enhanced supply of terrestrial organic matter recorded in the uppermost part of the Larrés Formation (Fig. 12). In the nearby Latas section, just 7 km to the NNW of Yebra de Basa, the MECO is also recorded by the progradation of the deltaic Sabiñánigo sandstone above the prodeltaic marls of the Larrés Formation, and is also manifested by a conspicuous increase in the percentage of reworked calcareous nannofossils in response to an enhanced hydrological cycle (Lasluisa et al., 2024). The coeval progradation of fluvial and deltaic sediments reported from the Olsón and Latas/Yebra de Basa sections has been taken as evidence for the isochronous progradation of the SPFB sedimentary systems in response to an intensified hydrological cycle during the MECO (Peris-Cabré et al., 2023). We identify the significant increase in the percentage of reworked calcareous nannofossils, the enhanced input of organic matter, and the occurrence of ferroan dolomitic concretions reported around the C18r/C18n boundary at the Izaga section as the sedimentological expression of such MECO-induced progradation in the deep sink of the basin (Fig. 12). From the late Lutetian to the early Bartonian, the SPFB underwent a period of continued flexural subsidence driven by tectonic loading along the northern fringe of the basin (Barnolas et al., 2019). This context of continued subsidence and creation of accommodation space was not favorable for the progradation of deltaic systems. Therefore, we consider that the deltaic progradation at different environments across the SPFB during the MECO (this work; Vinyoles et al., 2021; Peris-Cabré et al., 2023; Sharma et al., 2024; Lasluisa et al., 2024) leaves the acceleration of the hydrological cycle as its main underlying cause. The evident imprint of the MECO along a complete continental to deep marine transect across the SPFB reinforces the idea that the MECO exerted a more important influence on the environmental conditions of mid latitude settings than previously thought (Peris-Cabré et al., 2023).

Our results also indicate that the Sabiñánigo sandstone correlates with the uppermost part of the Larrés Formation to the west, and not with the Urroz limolites as has been classically assumed, which would explain the lack of a direct continuity between the Sabiñánigo and Urroz formations reported near the eastern termination of the Leire thrust (Puigdefábregas, 1975). These results imply that the Urroz limolites are located at a stratigraphic position similar to that of the Ezkaba turbidites in the western part of the basin (Payros et al., 1997), and are therefore more likely to represent the marginal part of a turbiditic system sourced from the northern side of the basin (Payros et al., 1997).

6. Conclusions

Our magnetobiostratigraphic study of the Izaga composite section indicates that the section spans from the uppermost part of C19r (ca. 41.3 Ma) in the latest Lutetian to the uppermost part of Chron C18n.2n (ca. 39.7 Ma) in the middle part of the Bartonian, and encompass calcareous nannofossil biozones CNE14 and CNE15. The record of Chron C19n at the Izaga composite section has been partially blurred due to the occurrence of slightly delayed magnetizations and could therefore not be clearly delineated as is commonly reported in other marine successions, including those previously proposed to host the Bartonian GSSP. Given its short duration, we envisage severe difficulties in finding a pristine record of C19n, which reinforces the idea that an alternative biostratigraphic event might need to be chosen as the primary marker of the Bartonian GSSP. We have identified the HO of *Sphenolithus*

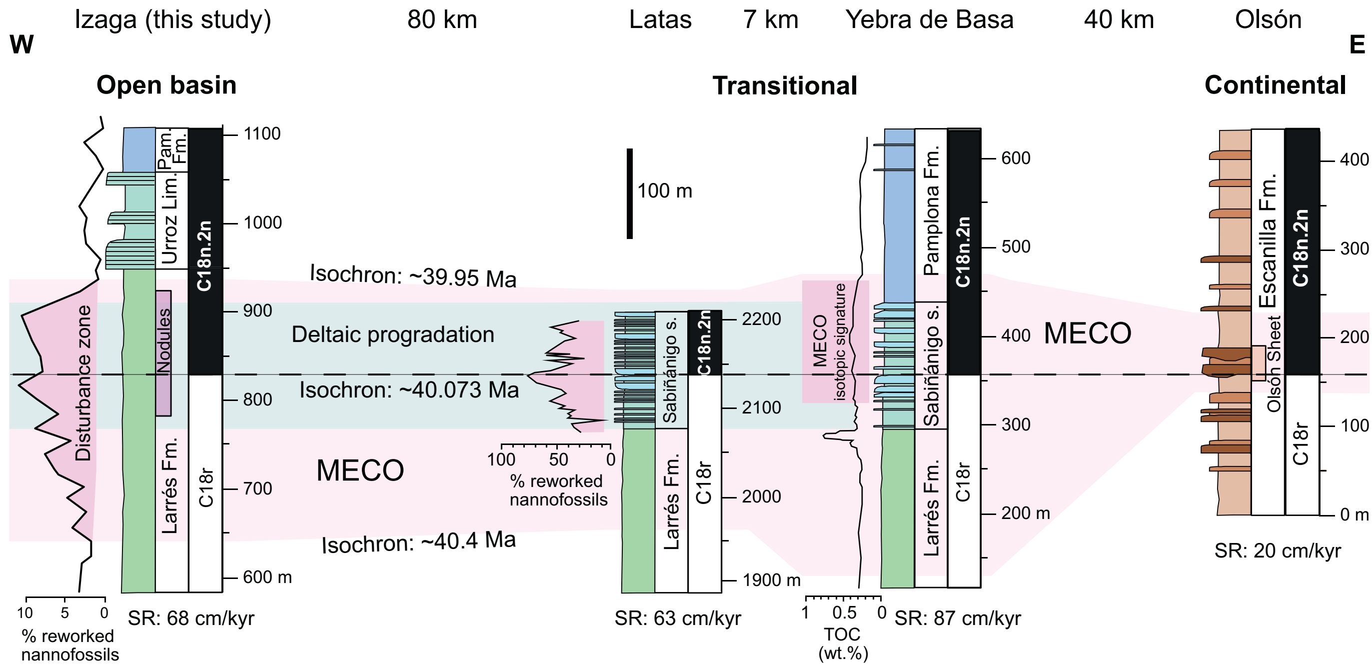

Fig. 12. W-E correlation panel across the South Pyrenean basin, showing the sedimentary expression of the MECO (pink shaded) and the associated deltaic progradation (blue shaded). Izaga section (this study); Latas section (Lasluisa et al., 2024); Yebra de Basa section (Peris-Cabré et al., 2023); Olsón section (Vinyoles et al., 2021). The overall increase observed in sedimentation rates (SR) along an E-W direction is only altered in the Yebra de Basa section, where significantly higher rates attest for the presence of the then active Oturia thrust (Vinyoles et al., 2021).

furcatolithoides B within chron C18r and at a close stratigraphic proximity to the top of Chron C19n, as has been also found in most sections worldwide. Based on this, we propose the HO of *Sphenolithus furcatolithoides* B as the most suitable biostratigraphic alternative to mark the base of the Bartonian Stage. If this proposal is accepted, the expanded nature of the succession (>1100 m), the dominance of fine-grained (marly) sedimentary facies, the superb outcrop conditions, and the accessibility to the area place the Izaga composite section as one of the best prospective successions to host the Bartonian GSSP.

Our results further reveal an interval of increased percentages in reworked calcareous nannofossils and more negative values of δ^{18}O and δ^{13}C, which concur with the presence of the methane-driven ferroan dolomitic concretions, around the boundaries between calcareous nannofossil zones CNE14/CNE15 and chrons C18r/C18n.2n. This indicates increased organic matter supply from the continent in response to an enhanced hydrological cycle during the MECO. These results demonstrate, along with results from neighbouring sections, that the sedimentological expression of the MECO is manifested along a complete continental to deep marine transect along the South Pyrenean foreland basin, and reinforces the idea that the MECO exerted a more important influence on the environmental conditions of mid latitude settings than previously thought.

Our age model constrains the emplacement of the Berroya megabreccia to the latest Lutetian (ca. 41.1 Ma), which indicates that the mechanism that triggered deposition of the South Pyrenean Eocene carbonate megabreccias persisted, at least, till the latest Lutetian. The age model also implies that the Urroz limolites do not correlate with the Sabiñánigo sandstone as has been classically assumed. This places the Urroz limolites at a stratigraphic position similar to that of the Ezkaba turbidites in the western part of the SPFB, and suggests that this formation does not represent the prodeltaic counterpart of a deltaic system prograding from the east but the marginal part of a turbiditic system sourced from the active northern fringe of the basin.

CRediT authorship contribution statement

P. Sierra-Campos: Writing – review & editing, Writing – original draft, Visualization, Validation, Supervision, Software, Methodology, Investigation, Formal analysis, Data curation, Conceptualization. **G. Bernaola:** Writing – review & editing, Writing – original draft, Methodology, Investigation, Formal analysis, Data curation. **P. Calvín:** Writing – review & editing, Visualization, Validation, Supervision, Software, Methodology, Investigation, Formal analysis, Data curation, Conceptualization. **M. Montes:** Writing – review & editing, Validation, Methodology, Investigation. **A. Luzón:** Writing – review & editing, Validation, Methodology, Investigation. **E. Bellido:** Writing – review & editing, Investigation. **A. Payros:** Writing – review & editing, Validation, Investigation. **E. Beamud:** Writing – review & editing, Supervision, Data curation. **B. Oliva-Urcia:** Writing – review & editing, Investigation. **E.L. Pueyo:** Writing – review & editing, Visualization, Validation, Supervision, Software, Resources, Project administration, Methodology, Investigation, Funding acquisition, Formal analysis, Data curation, Conceptualization. **J.C. Larrasoaña:** Writing – review & editing, Writing – original draft, Visualization, Validation, Supervision, Software, Resources, Project administration, Methodology, Investigation, Funding acquisition, Formal analysis, Data curation, Conceptualization.

Declaration of competing interest

The authors declare no competing interests.

Acknowledgements

This study was funded by project UKRIA-4D (PID2019-104693GB-I00) of the Spanish Ministry of Science and Innovation, "ERDF A way of making Europe", which covered the predoctoral contract of P. Sierra-Campos (PRE2020-092425) and also by the project KINETRANS (PID2024-157800NB-C21). P. Calvín acknowledges funding from FJC2019-041058-I (Ministerio de Ciencia e Innovación Spain) contract. G. Bernaola and A. Payros acknowledges support by the Consolidated

Research Group IT602-22 of the Basque Government. We thank the assistance of E. Iriarte and the personnel of the IsoTopik Laboratory of the University of Burgos for their help with the stable isotope analyses. We are also grateful to two anonymous reviewers for their constructive reviews and to R. L. Totten for editorial handling.

Appendix A. Supplementary data

Supplementary data to this article can be found online at https://doi.org/10.1016/j.palaeo.2025.113368.

Data availability

Supplementary material and data available in https://doi.org/10.5281/zenodo.15869136

References

Agnini, C., Fornaciari, E., Giusberti, L., Grandesso, P., Lanci, L., Luciani, V., Muttoni, G., Pälike, H., Rio, D., Spofforth, D.J.A., Stefani, C., 2011. Integrated bio-magnetostratigraphy of the Alano section (NE Italy): a proposal for defining the middle-late Eocene boundary. Geol. Soc. Am. Bull. 123, 841–872. https://doi.org/10.1130/B30158.1.

Agnini, C., Fornaciari, E., Raffi, I., Catanzariti, R., Pälike, H., Backman, J., Rio, D., 2014. Biozonation and biochronology of Paleogene calcareous nannofossils from low and middle latitudes. Newsl. Stratigr. 47, 131–181. https://doi.org/10.1127/0078-0421/2014/0042.

Aubry, M.P., 1998. Early Paleogene Calcareous nannoplankton evolution: a tale of climatic amelioration. In: Aubry, M.-P., Lucas, S., Berggren, W.A. (Eds.), Late Paleocene–early Eocene Biotic and Climatic Events in the Marine and Terrestrial Records. Columbia University Press, New York, pp. 158–201.

Barnolas, A., Teixell, A., 1994. Platform sedimentation and collapse in a carbonate-dominated margin of a foreland basin (Jaca basin, Eocene, southern Pyrenees). Geology 22, 1107–1110. https://doi.org/10.1130/0091-7613(1994)022<1107:PSACIA>2.3.CO;2.

Barnolas, A., Larrasoaña, J.C., Pujalte, V., Schmitz, B., Sierro, F.J., Mata, M.P., van der Berg, B.C.J., Pérez-Asensio, J.N., Salazar, A., Salvany, J.M., Ledesma, S., García-Castellanos, D., Civis, J., Cunha, P., 2019. Alpine foreland basins. In: Quesada, C., Oliveira, J.T. (Eds.), The Geology of Iberia: A Geodynamic Approach, 4. Springer Nature, pp. 7–59. https://doi.org/10.1007/978-3-030-11190-8_2.

Berggren, W.A., Kent, D.V., Swisher III, C.C., Aubry, M.P., 1995. A revised Cenozoic geochronology and chronostratigraphy. In: Berggren, W.A., et al. (Eds.), Geochronology, Time Scales and Global Stratigraphic Correlation. Society for Sedimentary Geology Special Publication, 54, pp. 129–212. https://doi.org/10.2110/pec.95.04.0129.

Bown, P.R., Dunkley Jones, T., 2012. Calcareous nannofossils from Paleogene equatorial Pacific (IODP Sites U1331-1334). J. Nannoplankton Res. 32, 3–51.

Bown, P.R., Young, J.R., 1998. Techniques. In: Bown, P.R. (Ed.), Calcareous Nannofossil Biostratigraphy, 1st ed. 1998. Chapman & Hall, London, UK, pp. 16–28.

Boya, S., 2018. El sistema deltaico de la arenisca de Sabiñánigo y la continentalización de la Cuenca de Jaca. Tesis doctoral. Universidad Autónoma de Barcelona, 208 p.

Bralower, T.J., Self-Trail, M.J., 2016. Nannoplankton malformation during the Paleocene-Eocene Thermal Maximum and its paleoecological and paleoceangraphic significance. Paleoceanography 31. https://doi.org/10.1002/2016PA002980.

Bybell, L.M., Self-Trail, J.M., 1995. Evolutionary, Biostratigraphic, and Taxonomic Study of Calcareous Nannofossils from a Continuous Paleocene–Eocene Boundary Section in New Jersey. Professional Pap. 1554. U.S. Geol. Surv, Washington, D. C, pp. 1–114.

Canudo, J.I., Molina, E., 1988. Biocronología con foraminíferos planctónicos de la secuencia deposicional de Jaca (Pirineo aragonés): Eoceno medio y superior. Congreso Geológico de España, Comunicaciones 1, 273–276.

Canudo, J.I., Molina, E., Riveline, J., Serra Kiel, J., Sucunza, M., 1988. Les événements biostratigraphiques de la zone prépyrénéenne d'Aragon (Espagne), de l'Eocène moyen à l'Oligocène inférieur. Rev. Micropaleontol. 31, 15–29 (In French).

Cardozo, N., Allmendinger, R.W., 2013. Spherical projections with OSXStereonet. Comput. Geosci. 51, 193–205. https://doi.org/10.1016/j.cageo.2012.07.021.

Channell, J.E.T., Galeotti, S., Martin, E.E., Billups, K., Scher, H.D., Stoner, J.S., 2003. Eocene to Miocene magnetostratigraphy, biostratigraphy, and chemostratigraphy at ODP Site 1090 (sub-Antarctic South Atlantic). Geol. Soc. Am. Bull. 115, 607–623.

Choukroune, P., 1992. Tectonic evolution of the Pyrenees. Annu. Rev. Earth Planet. Sci. 20 (1), 143–158.

Coccioni, R., Montanari, A., Boschi, S., Catanzariti, R., Frontalini, F., Jovane, L., Kochhann, M.V.L., Pelosi, N., Sabatino, N., Savian, J.F., Sprovieri, M., 2022. Integrated stratigraphy of the Lutetian–Priabonian pelagic section at Bottaccione (Gubbio, central Italy): A proposal for defining and positioning the Global Stratotype Section and Point (GSSP) for the base of the Bartonian Stage (Paleogene System, Eocene Series). In: Koeberl, C., Claeys, P., Montanari, A. (Eds.), From the Guajira Desert to the Apennines, and from Mediterranean Microplates to the Mexican Killer Asteroid: Honoring the Career of Walter Alvarez: Geological Society of America Special Paper 557, pp. 1–36. https://doi.org/10.1130/2022.2557(16).

Cotton, L., Rivero-Cuesta, L., Franceschetti, G., Iakovleva, A., Alegret, L., Dinarès–Turell, J., Hooker, J., King, C., Fluegeman, R., Stacy, Y., Monechi, S., 2021. Reassessing the Bartonian unit stratotype at Alum Bay (Isle of Wight, UK): An integrated approach. Newsl. Stratigr. 54, 17–42. https://doi.org/10.1127/nos/2020/0563.

D'Onofrio, R., Zaky, A.S., Frontalini, F., Luciani, V., Catanzariti, R., Francescangeli, F., Giorgioni, M., Coccioni, R., Özcan, E., Jovane, L., 2021. Impact of the Middle Eocene Climatic Optimum (MECO) on foraminiferal and calcareous nannofossil assemblages in the Neo-Tethyan Baskil section (eastern Turkey): paleoenvironmental and paleoclimatic reconstructions. Appl. Sci. 11, 1–25 doi:10.3390/app112311339.

Dawber, C.F., Tripati, A.K., Gale, A.S., MacNiocaill, C., Hesselbo, S.P., 2011. Glacioeustasy during the middle Eocene? Insights from the stratigtraphy of the Hampshire Basin, UK. Palaeogeogr. Palaeoclimatol. Palaeoecol. 300, 84–100.

Edgar, K.M., Wilson, P.A., Sexton, P.F., Gibbs, S.J., Roberts, A.P., Norris, R.D., 2010. New biostratigraphic, magnetostratographic and isotopic insights in the Middle Eocene Climatic Optimum in low latitudes. Palaeogeogr. Palaeoclimatol. Palaeoecol. 297, 670–682. https://doi.org/10.1016/j.palaeo.2010.09.016.

Fisher, R., 1953. Dispersion on a Sphere. Proc. R. Soc. A 217 (1130), 295–305. https://doi.org/10.1098/rspa.1953.0064.

Fornaciari, E., Agnini, C., Catanzariti, R., Rio, D., Bolla, E.M., Valvasoni, E., 2010. Mid-latitude calcareous nannofossil biostratigraphy and biochronology across the middle to late Eocene transition. Stratigraphy 7, 229–264.

Gandolfi, A., Giraldo-Gómez, V.M., Luciani, V., Piazza, M., Adatte, T., Arena, L., Brahimsamba, B., Fornaciari, E., Frijia, G., Kocsis, L., Briguglio, A., 2023. The Middle Eocene Climatic Optimum (MECO) impact on the benthic and planktic foraminiferal resilience from a shallow-water sedimentary record. Riv. Ital. Paleontol. Stratigr. 129 (3), 629–651. https://doi.org/10.54103/2039-4942/20154.

Gandolfi, A., Giraldo-Gómez, V.M., Arena, L., Luciani, V., Papazzoni, C.A., Pignatti, J., Piazza, M., Kocsis, L., Baumgartner, C., Briguglio, A., 2025. Diverse ecological responses of foraminifera to the Middle Eocene Climatic Optimum (MECO) in shallow-water settings (Provençal Domain, NW Italy). Palaeogeogr. Palaeoclimatol. Palaeoecol. 661, 112697. https://doi.org/10.1016/j.palaeo.2024.112697.

Garcés, M., López-Blanco, M., Valero, L., Beamud, E., Muñoz, J.A., Oliva-Urcía, B., Vinyoles, A., Arbués, P., Cabello, P., Cabrera, Ll, 2020. Paleogeographic and sedimentary evolution of the South Pyrenean foreland basin. Mar. Pet. Geol. 113, 104105. https://doi.org/10.1016/j.marpetgeo.2019.104105.

Giorgioni, M., Jovane, L., Rego, E.S., Rodelli, D., Frontalini, F., Coccioni, R., Catanzariti, R., Özcan, E., 2019. Carbon cycle instability and orbital forcing during the Middle Eocene Climatic Optimum. Sci. Rep. 9 (9357). https://doi.org/10.1038/s41598-019-45763-2.

González-Lanchas, A., Remacha, E., Oms, O., Sierro, F.J., Flores, J.A., 2019. Middle Eocene calcareous nannofossils in the Jaca transect (South-central Pyrenees Eocene Basin, Aragón river valley, Huesca). Span. J. Palaeontol. 34 (2), 229–240. https://doi.org/10.7203/sjp.34.2.16096.

Gonzalvo, C., 1992. Los foraminíferos planctónicos del tránsito Eoceno-Oligoceno: Bioestratigrafía y cronoestratigrafía. Tesis doctoral Universidad de Zaragoza, 202 pp.

Gonzalvo, C., 1997. Correlación Paleoceanográfica mediante foraminíferos planctónicos del tránsito Eoceno Medio-Eoceno Superior entre la Cordillera Bética y el Pirineo. Rev. Soc. Geol. Esp. 10 (1), 29–38.

Hooker, J.J., King, C., 2019. The Bartonian unit stratotype (S. England): assessment of its correlation problems and potential. Proc. Geol. Assoc. 130, 157–169.

Intxauspe-Zubiaurre, B., Martínez-Braceras, N., Payros, A., Ortiz, S., Dinarès-Turell, J., Flores, J.-A., 2018. The last Eocene hyperthermal (Chron C19r event, ~41.5 ma): Chronological and paleoenvironmental insights from a continental margin (Cape Oaymbre, N Spain). Palaeogeogr. Palaeoclimatol. Palaeoecol. 505, 198–216. https://doi.org/10.1016/j.palaeo.2018.05.044.

Izquierdo-Llavall, E., Aldega, L., Cantarelli, V., Corrado, S., Gil-Peña, I., Invernizzi, C., Casas, A.M., 2013. On the origin of cleavage in the Central Pyrenees: Structural and paleothermal study. Tectonophysics 608, 303–318. https://doi.org/10.1016/j.tecto.2013.09.027.

Izquierdo-Llavall, E., Sainz, A.C., Oliva-Urcia, B., Burmester, R., Pueyo, E.L., Housen, B., 2015. Multi-episodic remagnetization related to deformation in the Pyrenean Internal Sierras. Geophys. J. Int. 201 (2), 891–914. https://doi.org/10.1093/gji/ggv042.

Jovane, L., Florindo, F., Sprovieri, M., Pälike, H., 2006. Astronomic calibration of the late Eocene/early Oligocene Massignano section (central Italy). Geochem. Geophys. Geosyst. 7, Q07012. https://doi.org/10.1029/2005GC001195.

Jovane, L., Florindo, F., Coccioni, R., Dinarès-Turell, J., Marsili, A., Monechi, S., Roberts, A.P., Sprovieri, M., 2007. The middle Eocene climatic optimum event in the Contessa Highway section, Umbrian Apennines, Italy. Geol. Soc. Am. Bull. 119, 413–427. https://doi.org/10.1130/B25917.1.

Jovane, L., Sprovieri, M., Coccioni, R., Florindo, F., Marsili, F., Laskar, J., 2010. Astronomical calibration of the middle Eocene Contessa Highway section, 298. Earth and Planetary Science Letters, (Gubbio, Italy), pp. 77–88. https://doi.org/10.1016/j.epsl.2010.07.027.

Keeping, H., 1887. On the discovery of the *Nummulina elegans* zone at Whitecliff Bay, Isle of Wight. Geol. Mag. 4, 70–72.

Kirschvink, J.L., 1980. The least-squares line and plane and the analysis of palaeomagnetic data. Geophys. J. R. Astron. Soc. 62 (3), 699–718. https://doi.org/10.1111/j.1365-246X.1980.tb02601.x.

Krause, A.J., Sluijs, A., van der Ploeg, R., Lenton, T.M., Pogge von Strandmann, P.A.E., 2023. Enhanced clay formation key in sustaining the Middle Eocene Climatic Optimum. Nat. Geosci. **16**, 730–738 (2023). https://doi.org/10.1038/s41561-023-01234-y.

Labaume, P., Mutti, E., Seguret, M., Rosell, J., 1983. Megaturbidites carbonatés du basin turbiditique de l'Eocene inférieur et moyen sud-pyrénéen. Bull. Soc. Geol. Fr. 25, 927–941. https://doi.org/10.2113/gssgfbull.S7-XXV.6.927.

Labaume, P., Meresse, F., Jolivet, M., Teixell, A., Lahfid, A., 2016. Tectonothermal history of an exhumed thrust-sheet-top basin: an example from the south Pyrenean thrust belt. Tectonics 35, 1280–1313. https://doi.org/10.1002/2016TC004192.

Larrasoaña, J.C., Parés, J.M., Millán, H., Del Valle, J., Pueyo, E.L., 2003a. Paleomagnetic, structural, and stratigraphic constraints on transverse fault kinematics during basin inversion: the Pamplona fault (Pyrenees, north Spain). Tectonics 22 (6), 1071. https://doi.org/10.1029/2002TC001446.

Larrasoaña, J.C., Parés, J.M., Pueyo, E.L., 2003b. Stable Eocene magnetization carried by magnetite and iron sulphides in marine marls (Pamplona-Arguis Formation, southern Pyrenees, northern Spain). Stud. Geophys. Geod. 47, 237–254. https://doi.org/10.1023/A:1023770106613.

Larrasoaña, J.C., Pueyo, E.L., Parés, J.M., 2004. An integrated AMS structural, paleo- and rock-magnetic study of the Eocene marine marls from the Jaca-Pamplona basin (Pyrenees, N Spain): new insights into the timing of magnetic fabric acquisition in weakly deformed mudrocks. In: Martín-Hernández, F., Lüneburg, C.M., Aubourg, C., Jackson, M. (Eds.), Magnetic Fabric, Methods and Applications, 238. Geological Society, London, Special Publication, pp. 127–143. https://doi.org/10.1144/gsl.sp.2004.238.01.10.

Larrasoaña, J.C., Roberts, A.P., Musgrave, R.J., Gràcia, E., Piñero, E., Vega, M., Martínez-Ruiz, F., 2007. Diagenetic formation of greigite and pyrrhotite in marine sedimentary systems containing gas hydrates. Earth Planet. Sci. Lett. 261, 350–366. https://doi.org/10.1016/j.epsl.2007.06.032.

Lasluisa, E.R., Oms, O., Remacha, E., González-Lanchas, A., Blanchar-Roca, H., Flores, J. A., 2024. Nannofossils from the Middle Eocene Sabiñánigo Sandstone Formation in the Jaca Basin (southern Pyrenees): biostratigraphy and paleoenvironmental implications. J. Micropalaeontol. 43, 55–68. https://doi.org/10.5194/jm-43-55-2024.

Liu, Q., Roberts, A.P., Larrasoaña, J.C., Banerjee, S.K., Guyodo, Y., Tauxe, L., Oldfield, F., 2012. Environmental magnetism: Principles and applications. Rev. Geophys. 50, RG4002. https://doi.org/10.1029/2012RG000393.

Lowrie, W., 1990. Identification of ferromagnetic minerals in rock coercivity and unblocking temperature properties. Geophys. Res. Lett. 17, 159–162. https://doi.org/10.1029/GL017i002p00159.

Mangin, J.P., 1959–1960. Le Nummulitique sud-pyrénéen à l'ouest de l'Aragon. Pirineos, Jaca 51-58, 1–631.

Martí Bono, C., Plana, F., 1996. Concreciones carbonatadas en margas del eoceno. Consecuencias geomorfológicas. IV Reunión de Geomorfología (Grandal, A. y Pagés, J., Eds). Sociedad Española de Geomorfología, 605-615.

Martini, E., 1971. Standard Tertiary and Quaternary calcareous nannoplankton zonation. In: Farinacci, A. (Ed.), Proceedings, 2nd International Conference Planktonic Microfossils Roma: Rome (Edizioni Tecnoscienza), 2, pp. 739–785.

Mayer-Eymar, K., 1858. Versuch einer neuen Klassifikation der Tertiär-Gebilde Europa's. Verhandlungen der Schweizer Naturforschenden Gesellschaft für die Gesamten Naturwissenschaften Trogen 42, 165–199.

Messaoud, J.H., Thibault, N., Bomou, B., Adatte, T., Monkenbusch, J., Spangenberg, J.E., Aljahdali, H.M., Yaich, C., 2021. Integrated stratigraphy of the middle-upper Eocene Souar formation (Tunisian dorsal): implications for the Middle Eocene Climatic Optimum (MECO) in the SW Neo-Tethys. Palaeogeogr. Palaeoclimatol. Palaeoecol. 581. https://doi.org/10.1016/j.palaeo.2021.110639.

Millán, H., Pocoví, A., Casas, A., 1995. El frente de cabalgamiento surpirenaico en el extremo occidental de las Sierras Exteriores: sistemas imbricados y pliegues de despegue. Rev. Soc. Geol. Esp. 8 (1-2), 73–90.

Millán, H., Pueyo, E.L., Aurell, M., Luzón, A., Oliva, B., Martínez-Peña, M.B., Pocoví, A., 2000. Actividad tectónica registrada en los depósitos terciarios del frente meriodinal del Pirineo Central. Rev. Soc. Geol. Esp. 13, 279–300.

Montes, M., 2009. Estratigrafía del Eoceno-Oligoceno de la cuenca de Jaca (Sinclinorio del Guarga). Tesis doctoral. Colección de Estudios Altoaragones 59, 355 p.

Muñoz, J.A., 1992. Evolution of a continental collision belt: ECORS-Pyrenees crustal balanced cross-section. In: McClay, K.R. (Ed.), Thrust Tectonics. Springer, Dordrecht, pp. 235–246. https://doi.org/10.1007/978-94-011-3066-0_21.

Muñoz, J.A., 2002. The Pyrenees. In: Gibbons, W., Moreno, T. (Eds.), The Geology of Spain. The Geological Society, London, pp. 370–385.

Mutti, E., Luterbacher, H.P., Ferrer, J., Rosell, J., 1972. Schema stratigrafico e lineamenti di facies del Paleogene marino nella zona centralle sudpirenaica tra Tremp (Catalogne) e Pamplona (Navarra). Mem. Soc. Geol. Ital. 11, 391–416.

Norris, R.D., Wilson, P.A., Blum, P., the Expedition 342, 2014. Proceedings, 342. IODP, College Station, TX. https://doi.org/10.2204/iodp.proc.342.2014 (Integrated Ocean Drilling Program).

Ogg, J.G., Bardot, L., 2001. Aptian through Eocene magnetostratigraphic correlation of the Blake Nose Transect (Leg 171B), Florida continental margin. In: Kroon, D., Norris, R.D., Klaus, A. (Eds.), Proceedings of the Ocean Drilling Program, Scientific Results, 171B. Ocean Drilling Program, College Station, TX, pp. 1–58. https://doi.org/10.2973/odp.proc.sr.171b.104.2001.

Okada, H., Bukry, D., 1980. Supplementary modification and introduction of code numbers of the low-latitude coccolith biostratigraphic zonation (Bukry, 1973; 1975). Mar. Micropaleontol. 5, 321–325. https://doi.org/10.1016/0377-8398(80)90016-X.

Oliva-Urcia, B., Pueyo, E.L., Larrasoaña, J.C., 2008. Magnetic reorientation induced by pressure-solution; a potential mechanism for orogenic-scale remagnetizations. Earth Planet. Sci. Lett. 265, 525–534. https://doi.org/10.1016/j.epsl.2007.10.032.

Oliva-Urcia, B., Beamud, E., Arenas, C., Pueyo, E.L., Garcés, M., Soto, R., Valero, L., Pérez-Rivarés, F.J., 2019. Dating the northern deposits of the Ebro foreland basin, kinematics of the frontal deformation in the SW Pyrenees. Tectonophysics 765, 11–34. https://doi.org/10.1016/j.tecto.2019.05.007.

Oliva-Urcia, B., Larrasoaña, J.C., Travé, A., Garcés, M., Sierra-Campos, P., Pueyo, E.L., Calvín, P., 2024. Iron-carbonate concretions with inverse magnetic fabrics; a record of environmental changes in the middle Eocene marine marls of the Southern Pyrenees? J. Iber. Geol. (2024). https://doi.org/10.1007/s41513-024-00271-9.

Oms, O., Dinarès-Turell, J., Remacha, E., 2003. Magnetic stratigraphy from deep clastic turbidites: an example from the Eocene Hecho group (southern Pyrenees). Stud. Geophys. Geod. 47, 275–288. https://doi.org/10.1023/A:1023719607521.

Pälike, H., Lyle, M., Nishi, H., Raffi, I., Gamage, K., Klaus, A., the Expedition 320/321 Scientists, 2010. Proc. IODP, 320/321. Integrated Ocean Drilling Program Management International, Inc, Tokyo. https://doi.org/10.2204/iodp.proc.320321.103.2010.

Payros, A., 1997. El Eoceno de la Cuenca de Pamplona: estratigrafía, facies y evolución paleogeográfica. PhD Thesis. Basque Country University, Bilbao, Spain, 403 p.

Payros, A., Pujalte, V., Orue−Etxebarria, X., Baceta, J.I., 1997. A Bartonian channel-levee turbidite system in the Pamplona Basin: tectonic and paleogeographic implications. Geogaceta 22, 145–148.

Payros, A., Pujalte, V., Orue−Etxebarria, X., 1999. The South Pyrenean carbonate megabreccias revisited: new interpretation based on evidence from the Pamplona basin. Sediment. Geol. 125, 165–194. https://doi.org/10.1016/S0037-0738(99)00004-4.

Payros, A., Dinarès-Turell, J., Orue-Etxebarria, X., Monechi, S., Ortiz, S., Apellaniz, E., Bernaola, G., 2014. In: Rocha, R., et al. (Eds.), In Search of the Bartonian (Middle Eocene) GSSP (I): Potential in the Basque–Cantabrian and Aquitanian Basins (W Pyrenees). Springer International Publishing, Switzerland, pp. 79–83 (Strati 2013). https://doi.org/10.1007/978-3-319-04364-7_27.

Payros, A., Dinarès-Turell, J., Monechi, S., Orue-Extebarria, X., Ortiz, S., Apellaniz, E., Martínez-Braceras, N., 2015a. The Lutetian/Bartonian transition (middle Eocene) at the Oyambre section (Northern Spain): Implications for standard chronostratigraphy. Palaeogeogr. Palaeoclimatol. Palaeoecol. 440, 240–248. https://doi.org/10.1016/j.palaeo.2015.09.015.

Payros, A., Ortiz, S., Millán, I., Arostegi, J., Orue-Etxebarria, X., Apellaniz, E., 2015b. Early Eocene climatic optimum: Environmental impact on the North Iberian continental margin. Geol. Soc. Am. Bull. 127, 1632–1644. https://doi.org/10.1130/B31278.1.

Pedrera, A., García-Senz, J., Pueyo, E.L., López-Mir, B., Silva-Casal, R., Díaz-Alvarado, J., 2023. Inhomogeneous rift inversion and the evolution of the Pyrenees. Earth Sci. Rev. 104555. https://doi.org/10.1016/j.earscirev.2023.104555.

Perch-Nielsen, K., 1971. Elektronenmikroskopische Untersuchungen an Coccolithen und verwandten Formen aus dem Eozän von Dänemark. Det Kongelige Danske Videnskabernes-Selskabs Skrivter 18, 1–76.

Peris-Cabré, S., Valero, L., Spangenberg, J.E., Vinyoles, A., Verité, J., Adatte, T., Tremblin, M., Watkins, S., Sharma, N., Garcés, M., Puigdefàbregas, C., Castelltort, S., 2023. Fluvio-deltaic record of increased sediment transport during the Middle Eocene Climatic Optimum (MECO), Southern Pyrenees, Spain. Clim. Past 19, 533–554. https://doi.org/10.5194/cp-19-533-2023.

Peters, C., Dekkers, M.J., 2003. Selected room temperature magnetic parameters as a function of mineralogy, concentration and grain size. Phys. Chem. Earth 28, 659–667. https://doi.org/10.1016/S1474-7065(03)00120-7.

Plaziat, J.C., 1981. Late Cretaceous to Late Eocene palaeogeographic evolution of southwest Europe. Palaeogeogr. Palaeoclimatol. Palaeoecol. 36, 263–293. https://doi.org/10.1016/0031-0182(81)90110-3.

Prestwich, J., 1847. On the probable age of the London Clay, and its relations to the Hampshire and Paris Tertiary systems. Q. J. Geol. Soc. Lond. 3, 354–377.

Pueyo, E.L., Millán, H., Pocoví, A., 2002. Rotation velocity of a thrust: a paleomagnetic study in the External Sierras (Southern Pyrenees). Sediment. Geol. 146, 191–208. https://doi.org/10.1016/S0037-0738(01)00172-5.

Pueyo, E.L., Santolaria, P., Calvín, P., Casas, A.M., Sánchez, E., Oliva-Urcia, B., Silva-Casal, R., Scholger, R., Rubio, F., Rey-Moral, C., Rodríguez-Pintó, A., Ayala, C., Egli, R., Pocoví, A., 2025. in press. Vertical-axis rotations and salt tectonics in the southwestern Pyrenean termination. Geological Society of America Special Paper devoted to Roberto Molina-Garza. Edited by: Iriondo, A.; Lawton, T.; Geissman, J. et al.

Puigdefábregas, C., 1975. La sedimentación molásica en la Cuenca de Jaca. Monografías del Instituto de Estudios Pirenaicos. Número extraordinario de la revista Pirineos. CSIC-Instituto de Estudios Pirenaicos, Jaca, p. 104.

Ramón, M.J., Pueyo, E.L., Oliva-Urcia, B., Larrasoaña, J.C., 2017. Virtual directions in paleomagnetism: a global and rapid approach to evaluate the NRM components. Front. Earth Sci. 5, 8. https://doi.org/10.3389/feart.2017.00008.

Remacha, E., Picart, J., 1991. In: Colombo, F. (Ed.), El complejo turbidítico de Jaca y el delta de la Arenisca de Sabiñánigo. Excursión Guide Book, 8. Congreso del Grupo Español del Terciario. Vic Universitat de Barcelona, 1er. 116 p.

Remacha, E., Arbués, P., Carreras, M., 1987. Precisiones sobre los límites de la secuencia deposicional de Jaca. Evolución de las facies desde la base de la secuencia hasta el techo de la arenisca de Sabiñánigo. Bol. Geol. Min. 98, 40–48.

Remacha, E., Fernández, L.P., Maestro, E., Oms, O., Estrada, R., Teixell, A., 1998. Excursion A1. The Upper Hecho Group turbidites and their vertical evolution to deltas (Eocene, South-central Pyrenees). In: IAS 15th International Sedimentological Congress. Field Trip Guidebook, Alicante, Spain, pp. 1–25.

Remane, J., Bassett, M.G., Cowie, J.W., Gohrbandt, K.H., Lane, H.R., Michelsen, O., Naiwen, W., 1996. Revised guidelines for the establishment of global chronostratigraphic standards by the International Commission on Stratigraphy (ICS). Episodes 19, 77–81. https://doi.org/10.18814/epiiugs/1996/v19i3/007.

Roberts, A.P., Chang, L., Rowan, C.J., Horng, C.S., Florindo, F., 2011. Magnetic properties of sedimentary greigite (Fe3S4): An update. Rev. Geophys. 49, RG1002. https://doi.org/10.1029/2010RG000336.

Rodriguez-Pintó, A., Pueyo, E.L., Serra-Kiel, J., Samsó, J.M., Barnolas, A., Pocoví, A., 2012. Lutetian magnetostratigraphic calibration of larger foraminifera zonation

(SBZ) in the Southern Pyrenees: The Isuela section. Palaeogeogr. Palaeoclimatol. Palaeoecol. 333-334, 107–120. https://doi.org/10.1016/j.palaeo.2012.03.012.

Roigé, M., Gómez-Gras, D., Stockli, D.F., Teixell, A., Boya, S., Poyatos-Moré, M., 2023. Recycling effects in detrital zircon UPb signatures in a foreland basin: Identifying the multicyclic sediment sources of the Eocene-Miocene Jaca basin (southern Pyrenees, Spain). Sediment. Geol. 456, 106500. https://doi.org/10.1016/j.sedgeo.2023.106500.

Schmitz, B., Pujalte, V., 2003. Sea-level, humidity, and land-erosion records across the initial Eocene thermal maximum from a continental-marine transect in northern Spain. Geology 31 (8), 689–692. https://doi.org/10.1130/G19527.1.

Sharma, N., Spangenberg, J.E., Adatte, T., Vennemann, T., Kocsis, L., Vérité, J., Valero, L., Castelltort, S., 2024. Middle Eocene Climatic Optimum (MECO) and its imprint in the continental Escanilla Formation, Spain. Clim. Past 20, 935–949. https://doi.org/10.5194/cp-20-935-2024, 2024.

Sierra-Campos, P., Calvín, P., Izquierdo-Llavall, E., Pérez-Landazábal, J.I., Montes, M., Luzón, A., Bellido, E., Pueyo, E.L., Larrasoaña, J.C., 2025. Magnetic fabrics of weakly-deformed mudrocks from the Jaca-Pamplona basin (Pyrenees); new constrains on the sensitivity of magnetic fabrics and the tectonic evolution of the Southern Pyrenees. J. Iber. Geol. 51, 283–301. https://doi.org/10.1007/s41513-025-00288-8.

Silva-Casal, R., Aurell, M., Payros, A., Pueyo, E.L., Serra-Kiel, J., 2019. Carbonate ramp drowning caused by flexural subsidence: The South Pyrenean middle Eocene foreland basin. Sediment. Geol. 393–394, 105538. https://doi.org/10.1016/j.sedgeo.2019.105538.

Sluijs, A., Schouten, S., Donders, T.H., Schoon, P.L., Röhl, U., Reichart, G.J., Sangiorgi, F., Kim, J.H., Sinninghe Damsté, J.S., Brinkhuis, H., 2009. Warm and wet condi-tions in the Arctic region during Eocene Thermal Maximum 2. Nat. Geosci. 2, 777–780. https://doi.org/10.1038/ngeo668.

Speijer, R.P., Pälike, H., Hollis, C.J., Hooker, J.J., Ogg, J.G., 2020. The paleogene period. In: Gradstein, F., Ogg, J., Schmitz, M., Ogg, G. (Eds.), The Geologic Time Scale 2020, v. 2. Elsevier, Amsterdam, The Netherlands, pp. 1087–1140. https://doi.org/10.1016/B978-0-12-824360-2.00028-0.

Tauxe, L., Kylstra, N., Constable, C., 1991. Bootstrap statistics for paleomagnetic data. J. Geophys. Res. Solid Earth 96 (B7), 11723–11740. https://doi.org/10.1029/91JB00572.

Tauxe, L., Shaar, R., Jonestrask, L., Swanson-Hysell, N.L., Minnett, R., Koppers, A.A.P., Constable, C.G., Jarboe, N., Gaastra, K., Fairchild, L., 2016. PmagPy: Software package for paleomagnetic data analysis and a bridge to the Magnetics Information Consortium (MagIC) Database. Geochem. Geophys. Geosyst. 17 (6), 2450–2463. https://doi.org/10.1002/2016GC006307.

Toffanin, F., Agnini, C., Fornaciari, E., Rio, D., Giusberti, L., Luciani, V., Spofforth, D.J. A., Pälike, H., 2011. Changes in calcareous nannofossil assemblages during the Middle Eocene Climatic Optimum: clues from the central-western Tethys (Alano section, NE Italy). Mar. Micropaleontol. 81, 22–31.

Toffanin, F., Agnini, C., Rio, D., Acton, G., Westerhold, T., 2013. Middle Eocene to early Oligocene calcareous nannofossil biostratigraphy at IODP Site U1333 (equatorial Pacific). Micropaleontology 59, 1–14. https://www.jstor.org/stable/24413317.

van Dongen, B.E., Roberts, A.P., Schouten, S., Jiang, W.T., Florindo, F., Pancost, R.D., 2007. Formation of iron sulfide nodules during anaerobic oxidation of methane. Geochim. Cosmochim. Acta 71, 5155–5167. https://doi.org/10.1016/j.gca.2007.08.019.

Vinyoles, A., López-Blanco, M., Garcés, M., Arbués, P., Valero, L., Beamud, E., Oliva-Urcia, B., Cabello, P., 2021. 10 Myr evolution of sedimentation rates in a deep marine to non-marine foreland basin system: Tectonic and sedimentary controls (Eocene, Tremp–Jaca Basin, Southern Pyrenees, NE Spain). Basin Res. 33 (1), 447–477. https://doi.org/10.1111/bre.12481.

Westerhold, T., Röhl, U., 2013. Orbital pacing of Eocene climate during the Middle Eocene Climate Optimum and the chron C19r event: Missing link found in the tropical western Atlantic. Geochem. Geophys. Geosyst. 14 (11), 4811–4825. https://doi.org/10.1002/ggge.20293.

Zachos, J.C., Kroon, D., Blum, P., et al., 2004. *Proc. ODP, Init. Repts.,* 208. Ocean Drilling Program), College Station, TX. https://doi.org/10.2973/odp.proc.ir.208.2004.

Zijderveld, J.D.A., 1967. A.C. demagnetization of rocks: Analysis of results. In: Collinson, D.H., Runcorn, S.K., Creer, K.M. (Eds.), Methods in Palaeomagnetism: New York. Elsevier, pp. 254–286. https://www.mikrotax.org/Nannotax3/index.html. https://www.paleogene.org/working-group/bartonian/.